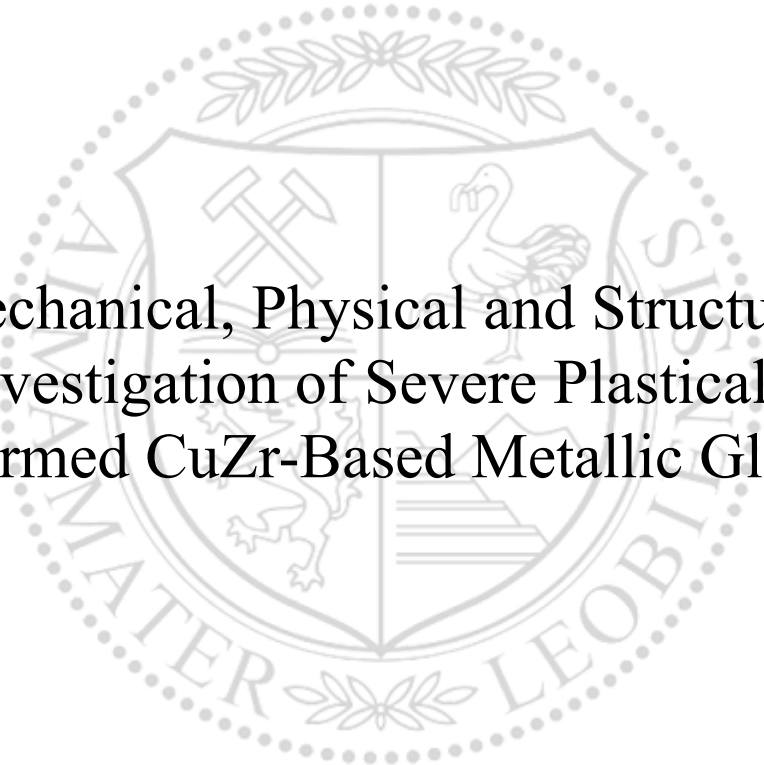




Montanuniversität Leoben

Master's Thesis



Mechanical, Physical and Structural
Investigation of Severe Plastically
Deformed CuZr-Based Metallic Glasses

Amir Rezvan

March 2019

Affidavit

I declare in lieu of oath, that I wrote this thesis and performed the associated research myself using only literature cited in this volume.

Leoben, March 2019

Amir Rezvan

Acknowledgements

Foremost, I would like to express my deepest gratitude and regards to my supervisor Prof. Jürgen Eckert, head of the Erich-Schmid-Institute of materials science, for giving me the opportunity to write my master thesis at his group and for his strong support during the whole course of this study.

I would like to express my sincerest appreciation and regards to Dr. Baran Sarac, whose unique vision and genuine directions assisted me utmost throughout my thesis.

I am also highly obliged to Dr. Jeongtae Kim, Dr. Viktor Soprunyuk, Dr. Christoph Gammer and all other staff at Erich-Schmid-Institute Leoben.

Special thanks to my family and friends for their love and support.

Abstract

This study shows processing of CuZr-based bulk metallic glass (BMG) via severe plastic deformation (SPD) under extreme loading condition, and investigates the effects of SPD induced by high-pressure torsion (HPT) on microstructural, thermal and (thermo)mechanical properties of $\text{Cu}_{46}\text{Zr}_{46}\text{Al}_8$ BMG. The influence of sub- T_g annealing and HPT treatment on the structure-property relationships of BMGs is assessed separately and alternately in reference to the as-cast state. High extent of applied shear strain during HPT generates free volume in the structure and has mechanical softening and structural rejuvenation effect against mechanical hardening and embrittlement of the glass induced by sub- T_g isothermal heat treatment (HT). Thermal properties, structural modifications, and surface morphology/compositional changes are investigated by differential scanning calorimetry, X-ray diffraction, and scanning/transmission electron microscopy, respectively. In general, this thesis aims for the enhancement of the intrinsic properties of CuZr-based BMGs via controlled nanocrystallization and their uniform distribution throughout the amorphous BMG matrix.

Abbreviations

ARB	Accumulative Roll Bonding
BF	Bright Field
BMG	Bulk Metallic Glasses
BMGC	Bulk Metallic Glass Composite
CCT	Continuous Cooling Transformation
DMA	Dynamic Mechanical Analysis
DSC	Differential Scanning Calorimetry
E'	Storage Modulus
E''	Loss Modulus
ECAP	Equal Channel Angular Pressing
EDX	Energy Dispersive X-ray
FESEM	Field Emission Scanning Electron Microscopy
FFT	Fast Fourier Transformation
FSDP	First Sharp Diffraction Peak
GFA	Glass Forming Ability
HPT	High-Pressure Torsion
HT	Heat Treatment
PIPS	Precision Ion Polishing System
SCLR	Supercooled Liquid Region
SPD	Severe Plastic Deformation
SPF	Superplastically Formable
SEM	Scanning Electron Microscopy
SSDP	Second Sharp Diffraction Peak
T_E	Eutectoid Transformation Temperature
T_g	Glass Transition Temperature
T_L	Liquidus Temperature
T_x	Temperature of Crystallization Onset
TEM	Transmission Electron Microscopy
XRD	X-ray Diffraction

Contents

Affidavit	i
Acknowledgements	ii
Abstract	iii
Abbreviations	iv
Contents	v
Chapter 1 – Introduction	1
Chapter 2 – Experimental	7
2.1 Casting of CuZr-based bulk metallic glass (BMG) discs	7
2.2 Sample preparation	8
2.3 X-ray diffraction and differential scanning calorimeter of the as-cast BMG Discs	8
2.4 Heat treatment (HT) of BMG discs	10
2.5 High pressure torsion (HPT) of BMG discs	10
2.6 Microhardness testing	11
2.7 Dynamic mechanical analysis	12
2.8 Thermal expansion measurement	14
2.9 Scanning electron microscopy	15
2.10 Transmission electron microscopy	15
Chapter 3 – Results and discussion	16
3.1 HPT and HT protocols of CuZr-BMG discs	16
3.2 Structural investigation of BMG discs	16
3.3 Thermal analysis of BMG discs	19
3.4 Influence of individual and combinatorial effect of HPT and HT	21
Chapter 3 – General conclusion and outlook	41
References	43

Chapter 1 - Introduction

Metallic glasses – also known as amorphous metals - are a new class of metals with extraordinary mechanical and magnetic properties [1-3]. Metals are in general crystalline. When metals are cooled from above their liquidus temperatures (T_L), they crystallize below the melting temperature. But if we cool them fast enough we can avoid the crystallization so that we freeze the liquid [4]. This means that the liquid becomes gradually slower in its mobility, and at some point on our time scale if we look at it, it just freezes there, that is what is called glass. If we make the glass out of metal it is called metallic glass and if we make the glass out of a combination of metals and/or metalloids with more elements, it is called bulk metallic glass (BMG) [5]. So we take the elements, we alloy them and by cooling them rapidly we create the bulk metallic glass. The defining characteristic of BMGs, which makes them different from conventional metallic materials, is the absence of crystallinity and the associated lack of microstructural features such as grain and phase boundaries [6]. BMGs with high strength (up to 6 GPa) and extensive elasticity (up to 2 %) [7, 8] have current and potential applications such as in space robotics as they do not become brittle in cold and show low friction and wear [9]. They are considered to be beneficial in recreational items because of the trampoline (bouncing) effect due to their ultra-high resilience of BMGs [10]. Metallic glasses are widely used as corrosion and wear-resistant coatings in heavy machinery (mining machinery, drilling machinery, etc.) [3, 11-14]. They can be exploited in precision tooling and high-end products [15]. A metallic glass blade can be sharpened to an exceptional edge, as there is no length scale above atomic to limit it [16]. These materials can also take the shape of a mold at very high precision using very small pressures in their supercooled liquid region [17-20]. In the following some of the important properties of BMGs regarding their present and potential applications are put together to give an introductory overview.

Table 1.1: General properties of CuZr-based BMGs [7].

Properties	Attractive	Unattractive
General	<ul style="list-style-type: none"> Absence of crystallinity and associated lack of microstructural features such as grain and phase boundaries, no features beyond near atomic scale 	<ul style="list-style-type: none"> Costs of components and processing
Mechanical	<ul style="list-style-type: none"> High Hardness H, high corrosion and wear resistance High yield strength σ_y High resilience σ_y^2/E 	<ul style="list-style-type: none"> Drastic localization of plastic flow into shear bands Embrittlement by annealing Limited process zone size
Thermal	<ul style="list-style-type: none"> Glass transition temperature T_g is mostly smaller than the temperature of crystallization onset T_x which enables processing in the supercooled liquid region 	<ul style="list-style-type: none"> Instability beyond T_c
Magnetic	<ul style="list-style-type: none"> High magnetic permeability 	<ul style="list-style-type: none"> Magnetic attributes have been already exploited for some decades
Processing	<ul style="list-style-type: none"> Low mechanical shrinkage and absence of grain structure allows high precision and excellent surface finish upon casting 	
Aesthetic	<ul style="list-style-type: none"> Absence of grain boundaries enables high-end polish, High durability Present novelty 	

BMGs accommodate plastic strain in highly localized shear bands, owing to absence of dislocations in their long range atomic structure [21]. Plasticity of metallic glasses can be enhanced by increasing the shear band density, which results in a homogenous deformation within the sample. It has been recently postulated that the interaction between shear bands and second phases plays an important role in stabilizing shear bands and inhibiting crack formation [22-27]. The shear bands could be stabilized as long as the spacing of the second phases is comparable with the plastic zone size (R_p) of the sample [23, 28]. More specifically, when the spacing of the second phases (crystalline dendrites, voids or spherulites) is equal or lower than the plastic zone size, shear bands will not immediately develop into cracks, but instead, the formation of multiple shear bands is triggered, and thus, energy dispersion due to stress concentration is favored. Moreover, it has been confirmed in the literature that plastic zone size of a variety of BMGs stays constant at elevated temperatures (at sub- T_g) [29]. CuZr-based metallic glasses are known to have plastic zone sizes of approximately 50 μm [30]. Thus, a bulk metallic glass composite (BMGC) with uniformly dispersed crystals in sizes of nano- to micro-scale particles will be beneficial for the enhancement of strength retention at temperatures close to glass transition.

Properties of metallic glasses are considered to be size-dependent (Figure 1.1). Samples with an effective thickness exceeding 1 mm exhibit often brittle deformation upon bending and tension. However they might show some compressive plasticity depending on the composition [31-34]. Multiple shear bands can be developed during compression of a monolithic BMG, especially in alloys with a low ratio of shear modulus to bulk modulus, which dramatically improves the plasticity of the sample [26, 28, 31]. When BMGs are used in geometries where one dimension is below about 10 times its critical crack length (about 1 mm for a medium range CuZr-based BMG), they show significant bending plasticity [1, 35, 36]. It has been proved by experiments [37, 38] that shear band confinement changes the deformation mode [24] as long as the spacing of the second phases matches the plastic zone size of the related BMG matrix.

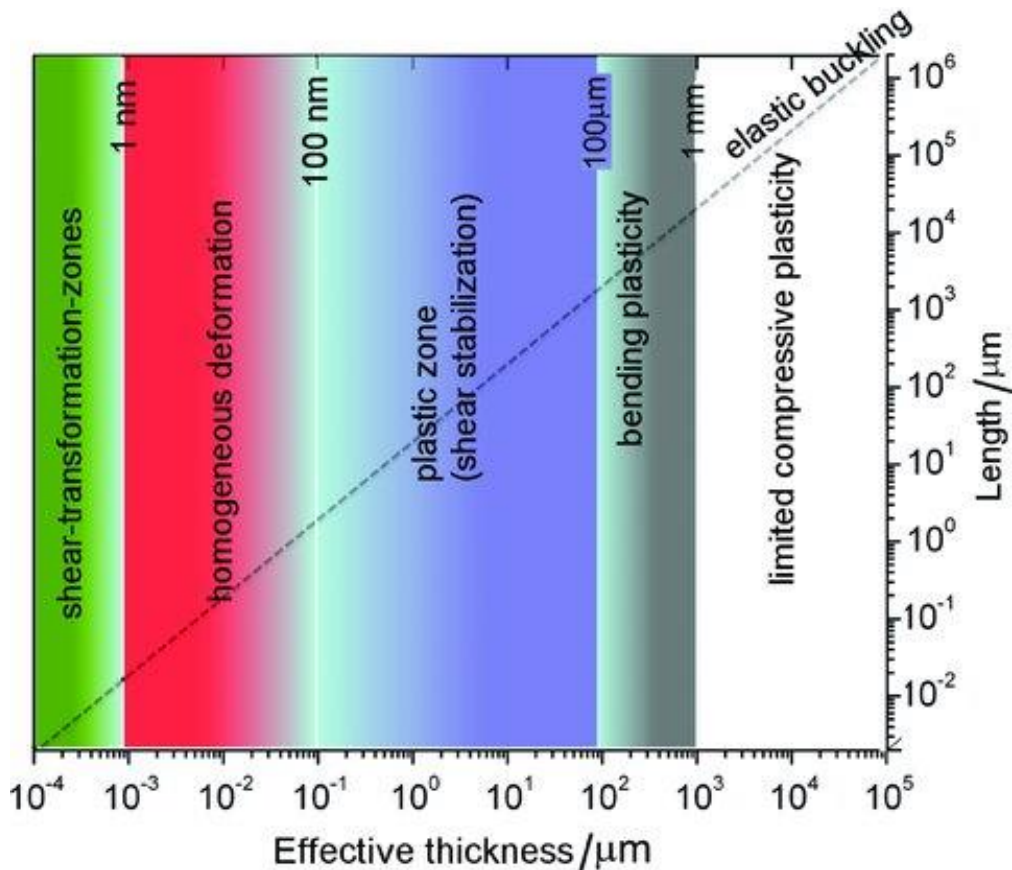


Figure 1.1: Size effects in metallic glasses, estimated for CuZr-based MG

Figure 1.2 illustrates the flow stress curves of different materials with respect to temperature change. The ideal processing zone is defined by the lowest processing pressure, by which turbulent flow and gravitational effects can be neglected on the time scale of the experiment. This region can be reached by plastics, which has led to the wide proliferation of plastics in industry. However, no conventional metals or even superplastically formable (SPF) alloys exhibit a comparable processing behaviour. The main disadvantage of plastics in structural applications is their low strength. On the contrary, metals exhibit high strength values, but are difficult to shape because of the abrupt change in viscosity around the melting temperatures. In comparison to plastics and high strength steels, BMGs with high processing behavior [39-43] exhibit room temperature strength that is two orders of magnitude higher than plastics and 2-3 times higher than conventional steels. Thus, BMGs possess the strength of metals with the processability of plastics [44, 45].

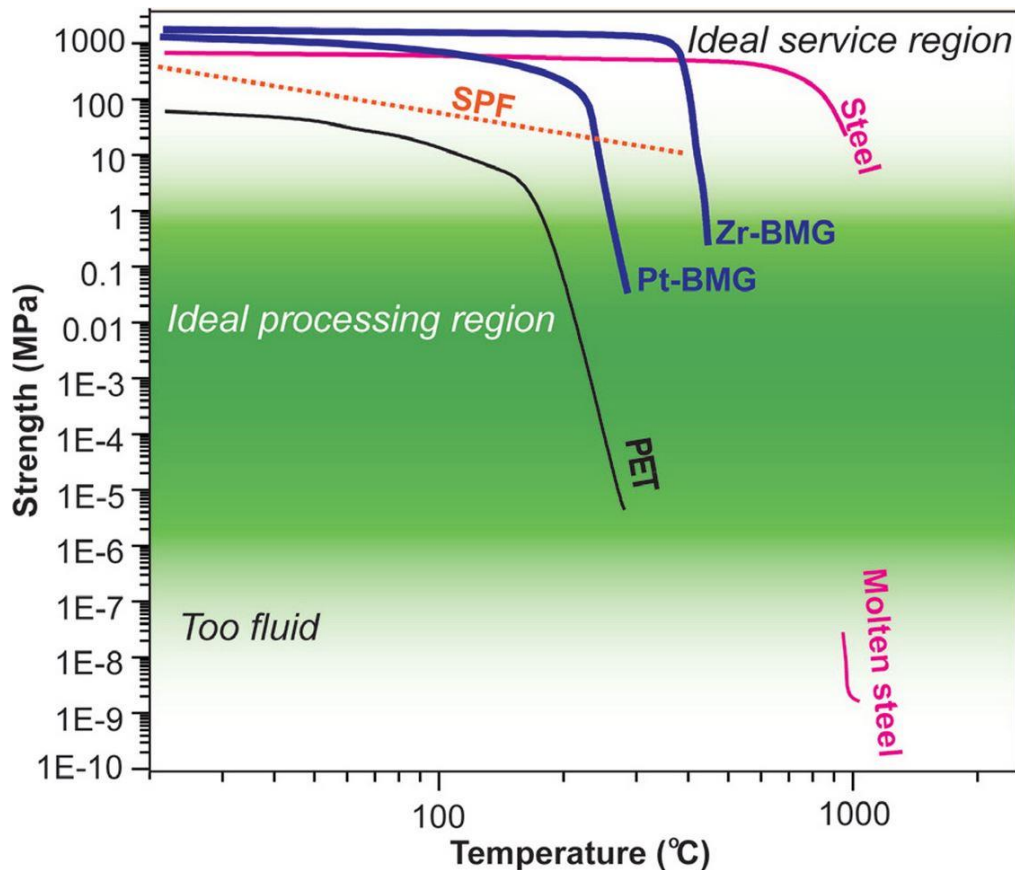


Figure 1.2 MGs combine two mutually exclusive attributes when they are thermoplastically formed: the strength of high strength metals, and the processability of plastics [44].

Severe plastic deformation (SPD) is an approach to improve strength and enhance ductility. High-pressure torsion (HPT) is one of the techniques which enables SPD up to 10000% strain [46]. Besides HPT there have been other techniques developed for SPD such as equal channel angular pressing (ECAP) or accumulative roll bonding (ARB). HPT method applies both pressure and torsion simultaneously on the sample [47]. Thus, this method has been considered as a suitable tool for inducing structural rejuvenation in the multicomponent advanced alloy systems, where the increase in plasticity is correlated with free volume generation. In this respect, Dmowski et al. proposed the idea that the rejuvenation via HPT can be accounted for the local heating in the shear bands in BMGs, and changes in short and long inter-atomic distances that lead to pronounced softening [48]. One big advantage about HPT is that the applied pressure on the sample is high and anisotropic which makes it possible to deform even brittle materials. The severe deformation is attributed to the fragility of the glass-forming liquid, where a more fragile liquid is likely to be more prone to structural rejuvenation [49]. Another important point is that the applied strain can be adjusted easily through number of turns. Aside from the bulk metal processing, HPT technique is used to consolidate the particles and to refine the microstructure (i.e. grain size refinement or re-distribution of the second phases), and thus, the intrinsic properties of

BMGs can be modified by putting them through shear strain under high hydrostatic pressure [50].

For CuZrAl BMG composites (BMGCs), desired B2-CuZr phase formation precipitates via polymorphous crystallization during cooling from the melt. The glass forming ability (GFA) of the remaining melt cannot then be kept high enough to form glassy matrix. The BMGCs containing the single B2-CuZr phase cannot be produced by an analogue semisolid casting system due to the solidification characteristic of CuZr-based alloy systems, whereas via copper mold suction casting technique it can be possible, by which the B2 phase volume is sensitized to the cooling rate [51, 52].

In this study we used another method to fabricate BMGCs by controlled crystallization of monolithic BMGs via sub- T_g heat treatment [53, 54]. This technique is composed of two steps: casting precursory fully amorphous BMGs and subsequent heat treatment on the precursors.

However, when the rod/plate diameter exceeds a certain dimension (e.g. 5 mm or higher), the experimental cooling rate becomes comparable to the critical cooling rate, leading to formation of crystals or defects (e.g. voids, irregular flow lines). Here, our target was to generate macroscopically fully-amorphous round plates with dimensions as high as possible (e.g. 40 mm in diameter), and investigate the influence of post-heat treatment and/or HPT on the overall properties of CuZr-BMGs.

Controlled nanocrystallization resulting from the annihilation of free volume is possible by short-term sub- T_g heat treatment [52, 55, 56]. Sub- T_g heat treatment improves the properties of the material by creating nucleation sites for nanocrystallization [52]. Pre-annealing drastically affects the rejuvenation and reduces the generated free volume which leads to restoration of high hardness and elastic modulus [57]. Nanocrystallization is achieved via heat treatment and HPT is used afterwards to disperse the nanocrystalline nuclei homogenously within the matrix. In this study we primarily show how nanocrystallization and structural reordering by HPT influence the final structural, mechanical and thermal properties of BMGs.

Chapter 2 – Experimental

2.1 Casting of CuZr-based Bulk Metallic Glass Discs

The master-alloy $\text{Cu}_{46}\text{Zr}_{46}\text{Al}_8$ has been casted using arc melting system AM0.5 from Bühler GmbH. The industrial constituents weighed by Sartorius Secura225D-1S scale with accuracy of 0.001g for their right proportions. Since GFA is low for this BMG alloy system to be able to produce rods of minimum 50 mm in height and 8 mm in diameter, a custom-built copper mold with circular plate geometry of 40 mm (fixed) in diameter and 2 mm (adjustable) in thickness was used.

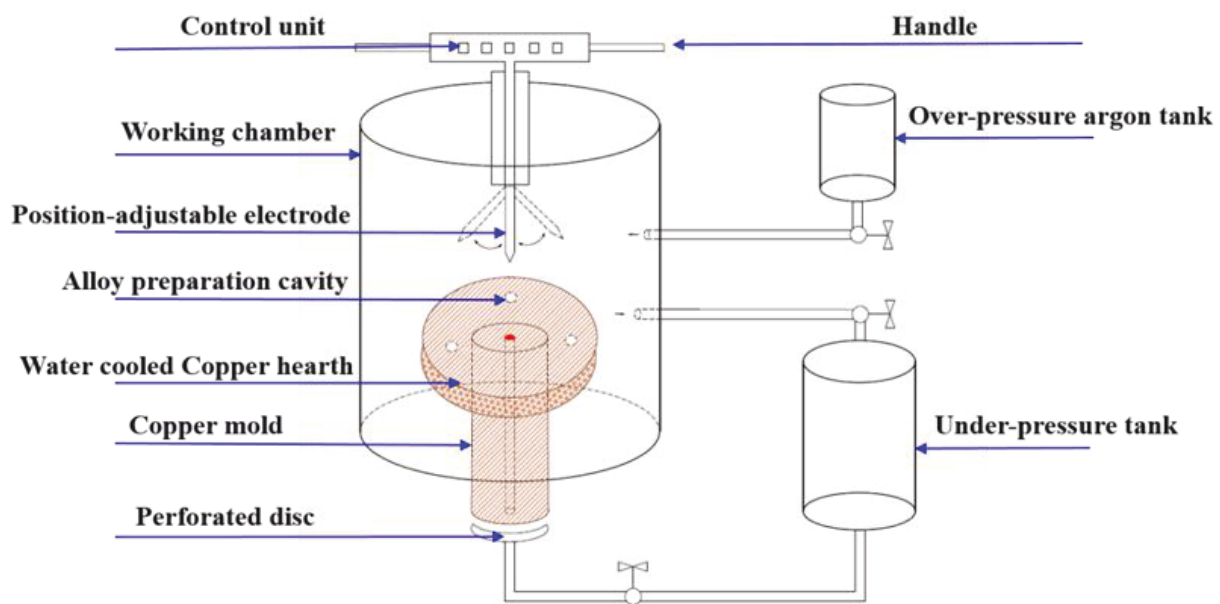


Figure 2.1: Illustration of arc melting device with a casting setup. Round disc (medallion) diameter of 40 mm, thickness of 2 mm [58].

The working chamber in this setup is connected with two pumps in series – one rotary and one diffusion pump. With these pumps we can evacuate the chamber down to 10^{-6} mbar in 30 minutes. A tungsten electrode is used to generate the arc. The current and the corresponding casting temperature can be adjusted by a power control unit. The melting current can go up to maximum of 400 A. First we melt the Ti getter to get rid of oxygen in the chamber, and subsequently we go onto raw materials and melt them to achieve a homogenous composition. To homogenize the ingot thoroughly, we repeated the melting five times. Once the master alloy is made we proceeded to make the bulk metallic glass via suction casting. Through pressure differential between the designed copper mold cavity and the working chamber under argon atmosphere we casted 2 mm thick amorphous plate with purity of higher than 99%. No grain boundaries and no defect were observed under optical microscope on the micro-scale. The exact chemical composition was verified by energy dispersive X-ray (EDX) attached to scanning electron microscope (SEM). Figure 2.2 shows an example BMG disc casted by the mentioned technique.

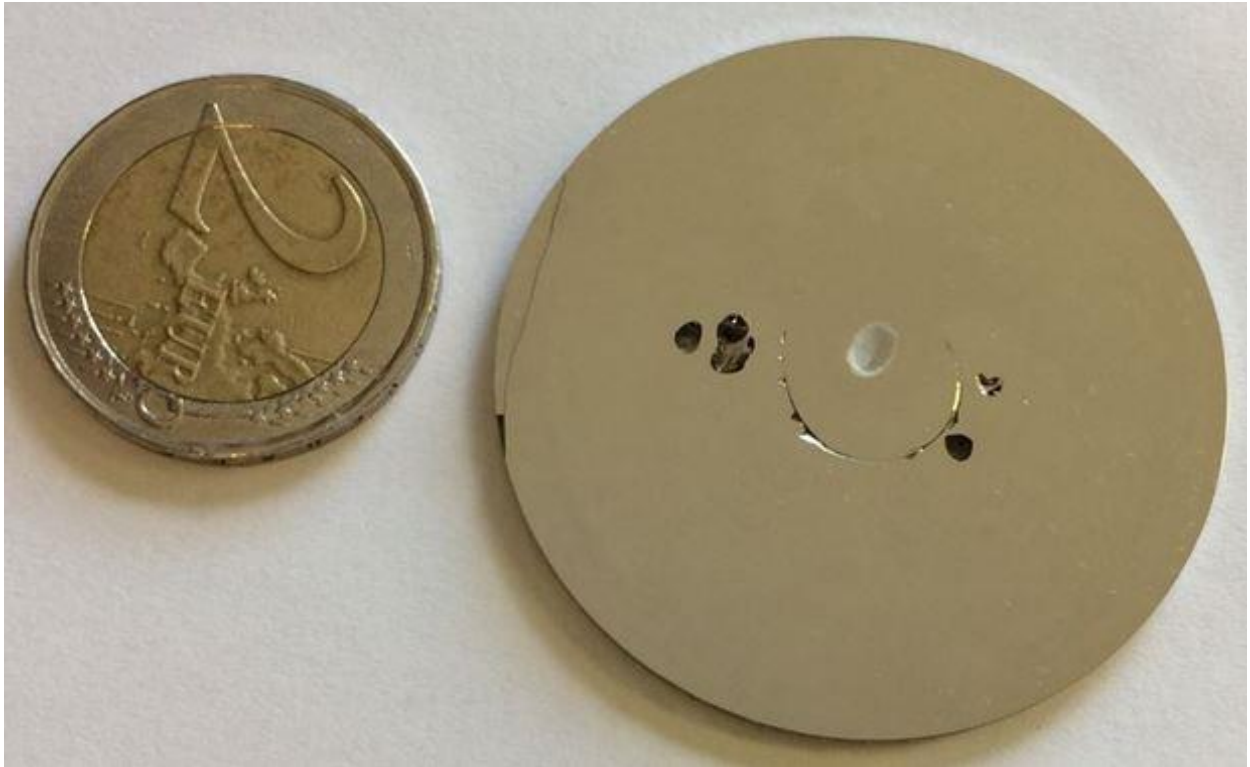


Figure 2.2: Medallion-shape BMG casted by suction casting - 40 mm in diameter, 2 mm in thickness

2.2 Sample Preparation

We cut 8 mm discs from the 40 mm casted plate using a custom-built electro discharge machine. The samples were ground and polished with slurry of diamond (9 mm particles) dispersed in water down to 1.00 ± 0.05 mm. The samples were subsequently rinsed in Isopropanol+acetone+water combination (each for 5 mins) and air-dried. Microporosity of the final discs was checked by Olympus Digital Microscope BX51.

2.3 X-ray Diffraction (XRD) and Differential Scanning Calorimeter (DSC) of the as-cast BMG discs

The specimens are checked in the XRD to make sure that they are fully amorphous and no crystallization has occurred during casting both along the radius and across the thickness of the samples (Figure 2.3). In XRD analysis (D2 phaser – Bruker) the broad peak is expected to be seen for the amorphous structures, as for the crystalline materials sharp peaks based on

the crystal structure and lattice specifications are observed. The casted BMG showed a broad diffraction pattern with first (FSDP) and second (SSDP) sharp diffraction peaks confirming the fully amorphous nature. To find the maximum peak positions, the curve fitting for the first diffraction peak was performed by Pseudo-Voigt function which is a convolution of Gaussian and Lorentzian peak fit. Non-diffracting substrates were used to avoid possible iron peaks from the holders.

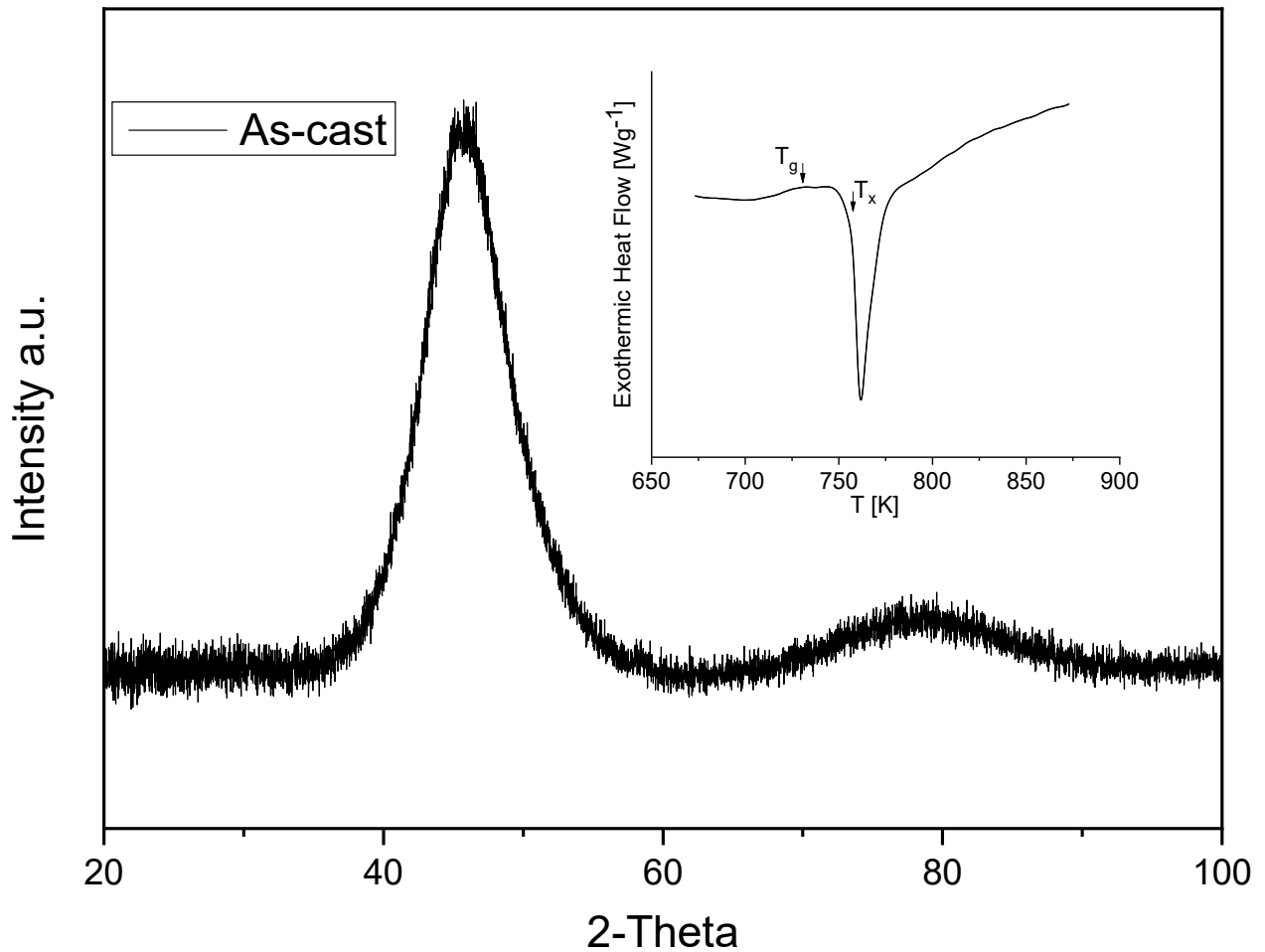


Figure 2.3: XRD pattern of the as-cast BMG plate and prepared BMG discs ($\text{Co } K_\alpha$ radiation = 1.7089 \AA at the step size of 0.02). The inset shows the DSC curve of the cast BMG.

Differential scanning calorimetry (DSC) tests were conducted using Mettler Toledo DSC 3+ under argon atmosphere at the constant heating rate of 10 K/min . The weight of the samples were selected as $15 \pm 1 \text{ mg}$. The samples were heated twice, and normalization was conducted by subtracting the baseline from the original heating curve. The cooling rate between two heating periods were selected as 50 K/min to minimize the influence of the time spent for cooling on the overall DSC data. A representative DSC analysis for the as-cast state is given in the inset of figure 2.3. Glass transition temperature (T_g) and temperature of crystallization onset (T_x) with a subsequent sharp drop in the exothermic heat flow can be

clearly observed. The presented data corroborates the fully amorphous state of the selected BMG.

2.4 Heat treatment of BMG discs

Four specimens were heated up in a mini-furnace separately to 623 K, 653 K, 683 K and 713 K at a rate of 10 K/s and kept isothermally for 15 minutes. The accuracy of the heating unit of the furnace is within $\pm 2\text{K}$. The specimens were immediately water quenched afterwards to the room temperature to avoid the post-crystallization effect. Similarly, we have heat treated 3 samples at the constant temperature of 683 K for 15, 30, 60 minutes followed by water quenching.

2.5 High-Pressure Torsion of BMG discs

The samples were at first sandblasted for 20 seconds which enabled uniform sand coating to avoid any slippage during HPT by increasing the friction between samples and anvils. The high-pressure torsion device is a custom built setup with a maximum load of 40 tones. The sample was placed between two anvils; the top one is fixed and applies the compressive stress, while the bottom anvil is rotating to bring torsion onto the sample. The disc-shaped samples were deformed between the anvils. Both anvils have cylindrical cavity, which allows both central positioning of the samples and the pressure to be hydrostatic. The depths of the cavities together must be smaller than the sample thickness; besides some height loss of the specimen during HPT must be considered.

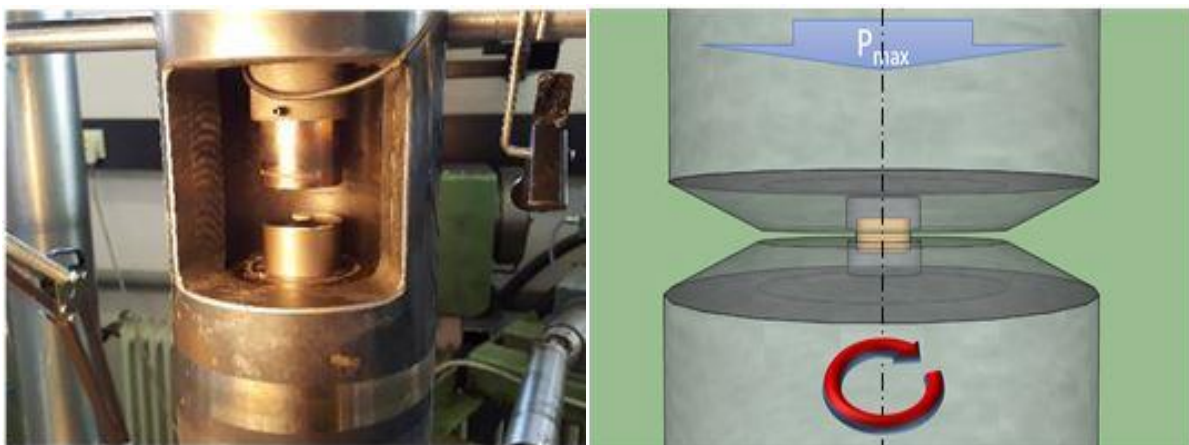


Figure 2.4: Illustration of an HPT setup

The HPT tests are conducted with the load of 7.8 GPa on the sample and rotation speed of 0.6 min^{-1} for the torsion. Anvils with cylindrical cavities of 8 mm and depth of 0.15 are used.

$$\text{Applied Shear Strain: } \gamma = \frac{2\pi Nr}{t} \quad (2.1)$$

N is number of turns, r is radius of the sample and t is thickness of the sample [59]. In HPT the torsion causes strain gradient along the radius – at the center the applied shear strain is theoretically zero, which means the very center undergoes nearly no deformation. The shear strain increases linearly with the radius towards the edges. Well machined anvils with high tolerances are required to establish a non-slippage condition which in turn enables a homogeneous deformation. Therefore, sandblasting of the cavity area is essential. This means that misalignment neither in cavity area nor in the surrounding area is permitted. Sandblasting of the cavity area is recommended.

We tried to find an optimized number of turns, and thus performed a series of HPT tests with different number of rotations to learn how the number of rotations will affect the hardness. HPTed samples were embedded and polished for hardness testing. We conducted the microindentation tests along the diameter. Observing no considerable changes in the mechanical properties of the material by increasing number of turns beyond 30 indicates the saturation of hardness resulting from reaching minimum grain sizes is reached. Comparing the results with the values of hardness for CuZr-based glass in the literature led us to set 30 turns for the series of the HPT tests [50], by which a saturation of HPT-induced dilatation (i.e., creation of free volume) is reached revealing that an equilibrium between creation and annihilation of free volume is established [60]. Annihilation is due to the local temperature rise during HPT [61].

For the HPT testing the samples were separately placed into the cavity of the lower anvil, and the upper anvil was gradually brought down till it touched the sample. The pressure was increased to the maximum of 7.8 GPa at a rate of 0.2 GPa per second. Next, the bottom anvil rotated at an angular speed of 0.6 min^{-1} for 50 minutes to complete the considered 30 turns. The average thickness of HPTed samples was $0.7 \pm 0.2 \text{ mm}$.

2.6 Microhardness testing

Vickers hardness measurement was conducted on the embedded samples using a Buehler Micromet 5104. The hardness values at each distance from the center were obtained along two perpendicular diagonals of the discs. The Vickers hardness is calculated by the applied force divided over the surface area of the indent. Thereby, the hardness is measured by the diagonal indents from 4 different points and averaged, whereas the error percent is determined by the standard deviation. To check how consistent the homogeneity of

deformation within samples is, we repeated all the tests 3 times, and almost same hardness profile for each case was observed. An error of 1% for the hardness measurements is determined.

2.7 Dynamic Mechanical Analysis

Dynamic mechanical analysis (DMA) was conducted at the same constant heating rate of 10 K/min using Discovery HR-3 (TA Instruments, the viscosity is subsequently calculated via the Stefan's equation [62, 63]. The chamber was purged with N_2 gas continuously upon heating and cooling. 10 N force is applied (25% static, 75% dynamic load), single frequency of one cycle per second (1 Hz) is used. The samples were heated from room temperature to 850 K . The experiment was performed in a displacement-controlled mode with $5\text{ }\mu\text{m}$ displacement at each sinusoidal loading intervals.

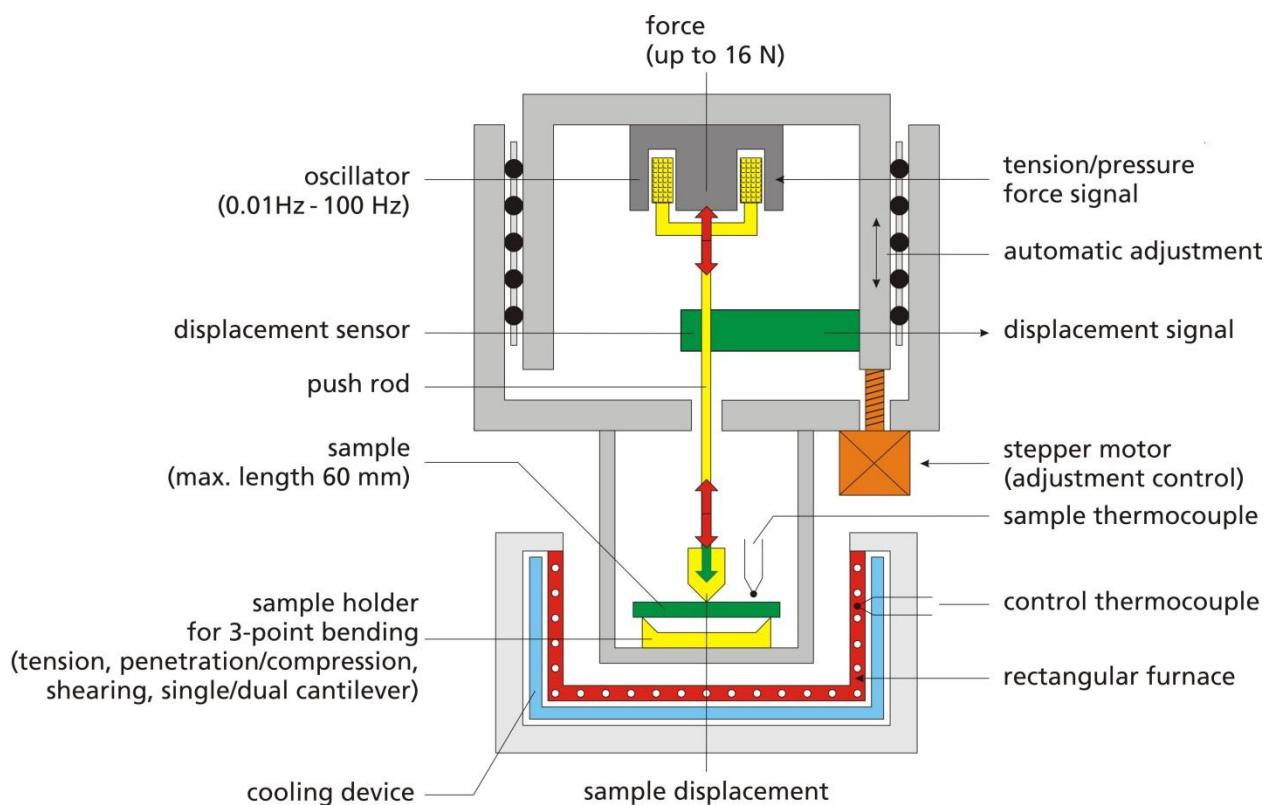


Figure 2.5: Schematic of a typical DMA setup

In a dynamical mechanical measurement, the sample is subjected to a sinusoidal stress (σ) as shown in figure 2.5. The resulting strain (ϵ) is also sinusoidal with the same frequency, but with a lag in the phase.

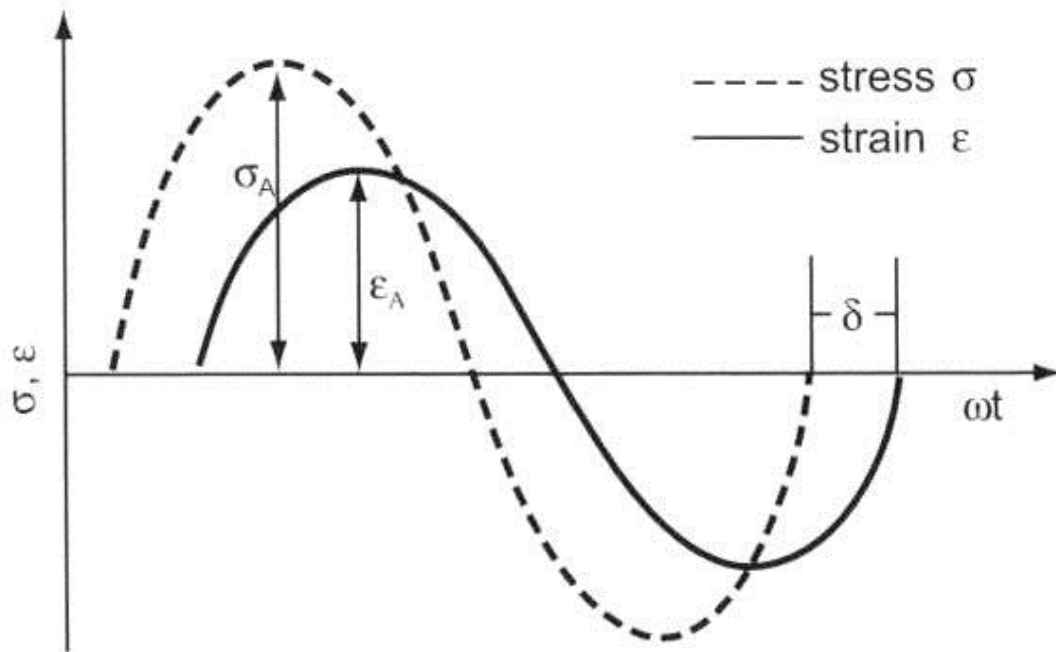


Figure 2.6: Principles of dynamical mechanical testing showing sinus-shaped oscillation and answer signal of a linear viscoelastic material

This material behaviour can be described as follows.

$$\delta = \delta_0 e^{i\omega t}, \quad (2.2)$$

$$\epsilon = \epsilon_0 e^{(i\omega t - \delta)}, \quad (2.3)$$

$$E^* = \frac{\delta(\omega)}{\epsilon(\omega)} = \frac{\delta_0}{\epsilon_0} \cos\delta + i \sin\delta, \quad (2.4)$$

$$E^* = E' + iE'' \quad (2.5)$$

$$\tan\delta = \frac{E''}{E'} \quad (2.6)$$

Storage modulus (E') represents the material's stiffness and is proportional to the maximum stored work during stress. Loss modulus (E'') is proportional to the work dissipated from the material during stress. It is a measure for the oscillation energy transformed into heat. Loss factor ($\tan \delta$) represents the mechanic damping or inner friction of a viscoelastic system. A high loss factor represents a high non-elastic deformation part, whereas a low loss factor a more elastic material.

2.8 Thermal Expansion Measurement

A dilatometer (parallel plate rheometer) is used to measure dimensional changes in the differently treated samples as a function of temperature. Here, Thermal expansion/contraction $\Delta L/L_0$ is measured under constant load of 50 mN and at heating rate of 10 K/min. Figure 2.7 illustrates a typical dilatometer.

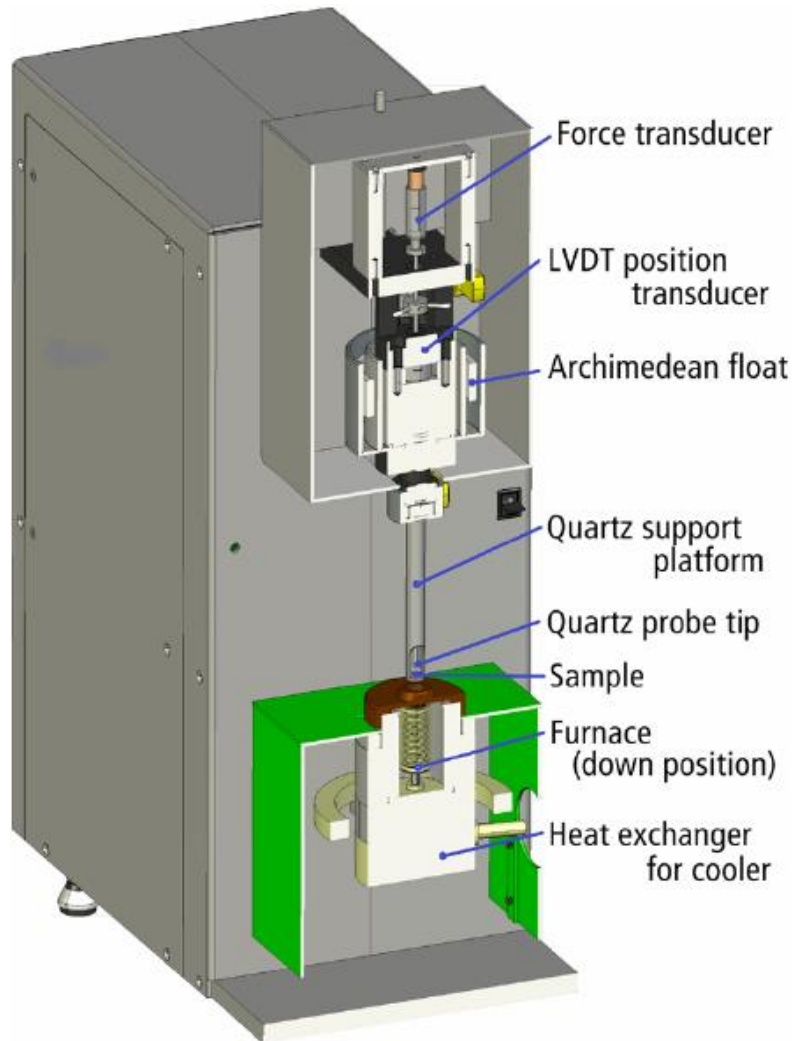


Figure 2.7: Cross section illustration of dilatometer showing functional components.

2.9 Scanning Electron Microscopy

Evolution of structural modifications of the differently treated samples are investigated in a field emission scanning electron microscopy (FESEM – Zeiss LEO1525) with a Schottky emitter in reference to the as-cast. The acceleration voltage was selected as 20 kV. System vacuum was 10^{-4} mbar. Four quadrant back scatter detector was utilized to determine the phase contrast of the nanocrystals. Energy dispersive X-ray spectrometer (EDX) with a point resolution of 2 nm was used for the compositional analysis. SEM was performed on the cross section of the samples. The elemental composition of the visualized regions was analyzed by energy dispersive x-ray spectroscopy (EDX) attached to SEM.

2.10 Transmission Electron Microscopy

Disc shaped transmission electron microscopy (TEM) samples were sliced from the BMG specimens and thinned down to electron transparency using a precision ion polishing system (PIPS). Ion milling was conducted at low energies using liquid nitrogen cooling (down to 213 K) to eliminate heating upon sample preparation. The prepared TEM samples are all electron transparent (thickness below 50 nm). The TEM analyses were conducted using a JEOL 2100F operated at 200 kV and Philips TEM CM12 at 120 kV. The TEM was equipped with an imaging spherical aberration corrector (CEOS) for HRTEM imaging. The nanodiffraction patterns (2004×1336 pixels in size) were acquired with a Gatan Orius CCD using an exposure time of 2 s.

Chapter 3 - Results and Discussion

3.1 HPT and HT Protocols of CuZr-BMG Discs

The different specimens investigated (i.e., as-cast specimens, deformed discs with different pre-annealing protocols, heat treated samples and deformed samples with post-annealing treatment (samples 1 – 10)) are summarized in table 3.1 for easier orientation.

Table 3.1. Samples of as-cast state and treated under different conditions

Sample #	Sample State	Sample #	Sample State
Sample 1	As-cast	Sample 6	713K 15min HT + HPT
Sample 2	RT HPT	Sample 7	683K 30min HT + HPT
Sample 3	623K 15min HT + HPT	Sample 8	683K 1h HT + HPT
Sample 4	653K 15min HT + HPT	Sample 9	HPT + 683K 15min HT
Sample 5	683K 15min HT + HPT	Sample 10	683K 15min HT

Sample 2 is HPTed at room temperature to show the effect of HPT primarily in comparison to sample 1 which is in the as-cast state. Samples 3 - 6 are heat treated separately in the furnace for 15 minutes at different temperatures below and around calorimetric T_g (623 K, 653 K, 683 K and 713 K) and subsequently deformed in the HPT machine, whereas samples 7 and 8 are heat treated separately in the furnace at 683 K for different durations (30min and 1h). For sample 9, in comparison to sample 5, we took the alternate order, by which the sample got deformed in the HPT first and then heat treated in the same condition as for the sample 5. Sample 10 is annealed in the heating unit at 683 K for 15 minutes to identify the influence of heat treatment.

3.2 Structural Investigation of BMG Discs

Samples 1 - 10 were ground and polished down to 0.3 mm equally from both sides. Samples were cleaned with acetone, ethanol and DI water. No microcrack was observed on the samples confirmed by an optical microscope. The heat treated samples with post-HPT (sample 3 – 8) were first investigated in the XRD. The results of XRD were grouped together in the Figures 3.1 and 3.2.

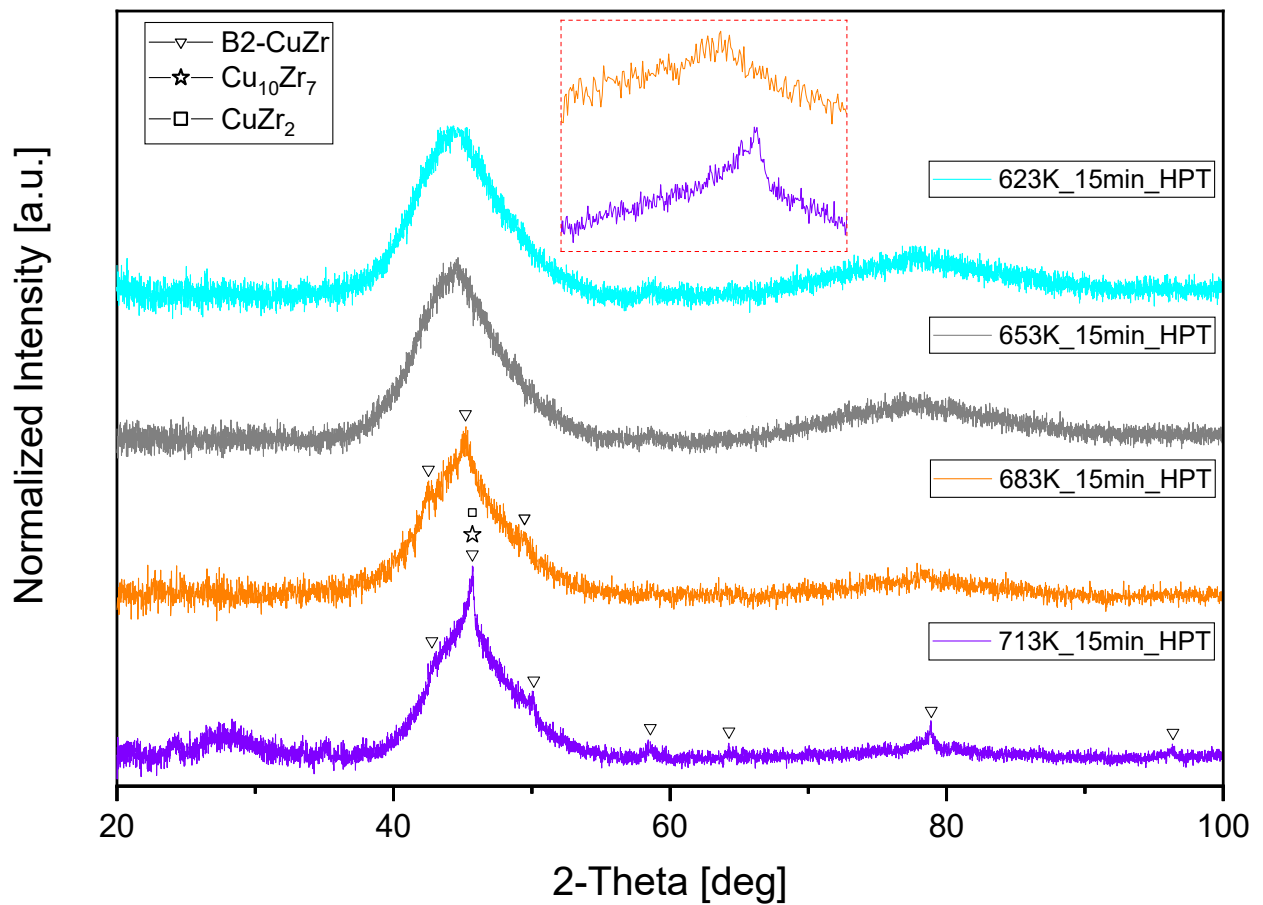


Figure 3.1: Comparison of XRD data of the deformed samples (samples 3 – 6) with different pre-annealing protocols (623K-15min-HT + HPT, 653K-15min-HT + HPT, 683K-15min-HT + HPT, 713K-15min-HT + HPT (samples 3 - 6)). Enlarged broad diffraction maxima of samples 5 and 6 are indicated in the red box.

We first considered pre-HT + post-HPT treatment to achieve nanocrystallization by controlled annealing and dispersion of nanocrystalline particles subsequently via HPT. Therefore, two series of tests were conducted to find out an optimized temperature and timing for the best tuning of properties. First four samples were heated isothermally at 623 K, 653 K, 683 K and 713 K for 15 minutes (figure 3.1). A crystalline peak corresponding to the cubic primitive B2-CuZr (Pm-3m) phase superimposed on the broad amorphous maximum appeared for the 683 K sample, whereas the crystalline peak on the broad diffuse maximum of the 713 K sample can be allocated to a mixture of crystalline structure consisting of B2-CuZr, $\text{Cu}_{10}\text{Zr}_7$, CuZr_2 [52], which is sharper and does not suit our tuning as it indicates existence of bigger crystals in the structure. Moreover, a eutectoid reaction from the primary metastable B2 phase to low temperature equilibrium phases, $\text{Cu}_{10}\text{Zr}_7$ primarily and CuZr_2 , occurred for the 713 K sample. For 653 K nearly no change was observed compared to the as-cast sample. A shift of maximum of the FSDP to higher degrees gradually from 623 K to 713 K is observed.

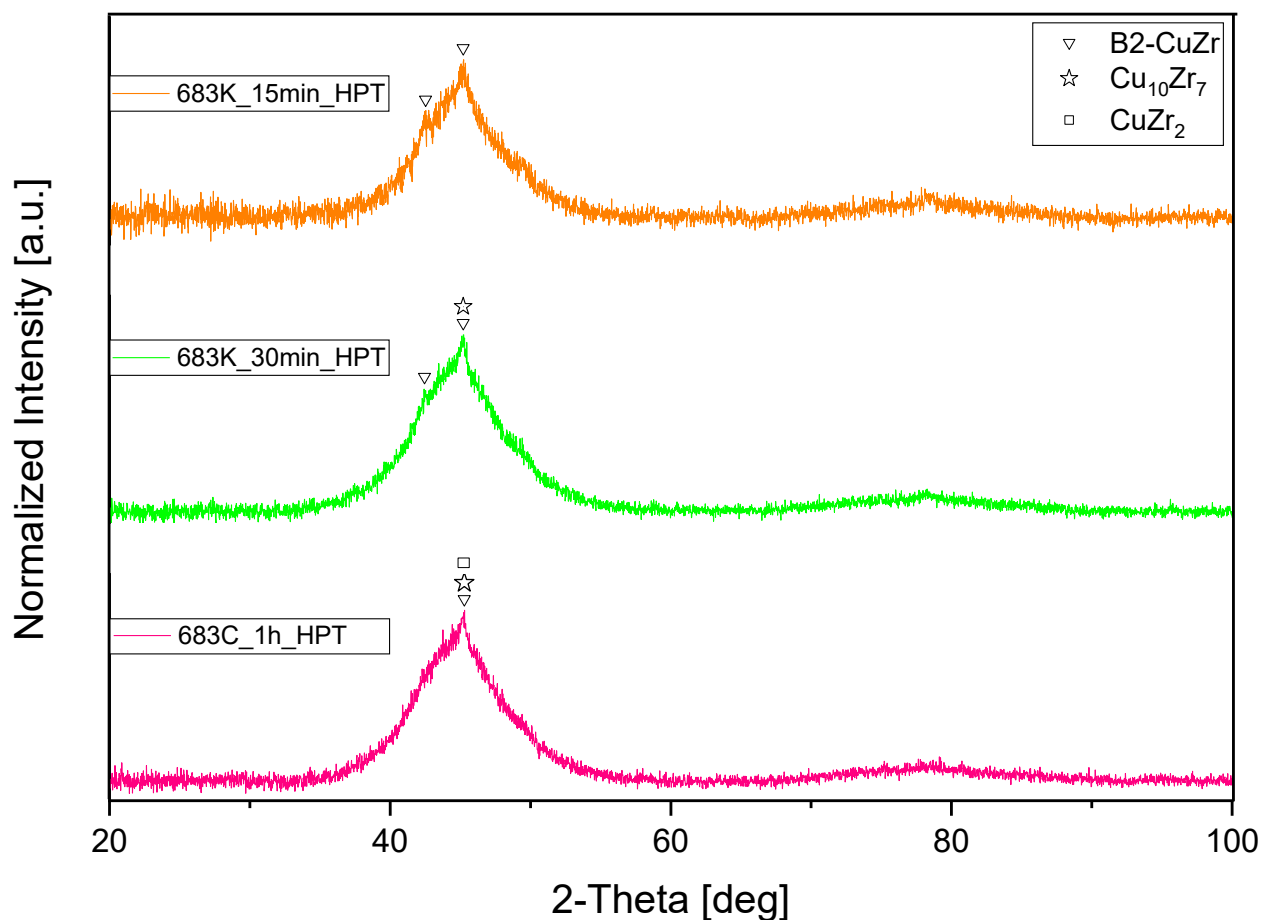


Figure 3.2: XRD measurements of the samples 5, 7 and 8 (683K-15min-HT + HPT, 683K-30min-HT + HPT, 683K-1h-HT + HPT)

After determining the onset of remarkable crystallization in XRD, the temperature is set constant to 683 K, and further by increasing the annealing time to 30 and 60 minutes the relative intensities of the crystalline diffraction peak on the broad amorphous scattering maximum are increased and the peak became slightly sharper (figure 3.2). Furthermore, the slight shoulder on the left-side of the broad halo becomes more pronounced upon longer annealing timing.

3.3 Thermal Analysis of BMG Discs

Pieces at larger radius were cut from the discs using wire saw device and placed into DSC after routine cleaning. The DSC samples are listed in the Table 3.2. Together with their thermal data to show the comparison. The DSC results are put together in figures 3.3 and 3.4.

Table 3.2: Post-HPTed samples with different pre-annealing treatments together with the thermal data. The temperature and crystallization enthalpy accuracy of the DSC analysis is within ± 0.5 K and ± 0.2 Wg⁻¹, respectively. T_g = glass transition temperature, T_x = crystallization temperature, ΔT = supercooled liquid region and ΔH_x = normalized crystallization enthalpy.

Sample	T_g (K)	T_x (K)	ΔT	ΔH_x (W/g)
623K 15min HT + HPT	718,8	756,5	37,7	50,0
653K 15min HT + HPT	720,1	757,3	37,2	58,1
683K 15min HT + HPT	722,1	757,2	35,1	57,1
713K 15min HT + HPT	711,8	741,0	29,2	34,9
683K 30min HT + HPT	718,7	759,0	40,3	50.8
683K 1h HT + HPT	720,1	758,4	38,3	40

Here we started observing modification first for the sample 5 (683K 15min HT + HPT) as in the XRD, whereas thermal characteristics for the 3rd and 4th samples are nearly the same as for the as-cast sample (Figure 2.3 inset). For the sample 5 a shoulder described by the deconvolution peak starts to emerge, whereas for the sample 6 crystallization starts to dominate, which results in the dramatic drop in the ΔH_x along with the decrease in the T_g , T_x and ΔT . Sample 6 is crystallized beyond the nucleation-controlled crystallization aimed by this study. The double peak of crystallization is a result of compositional segregation [64, 65].

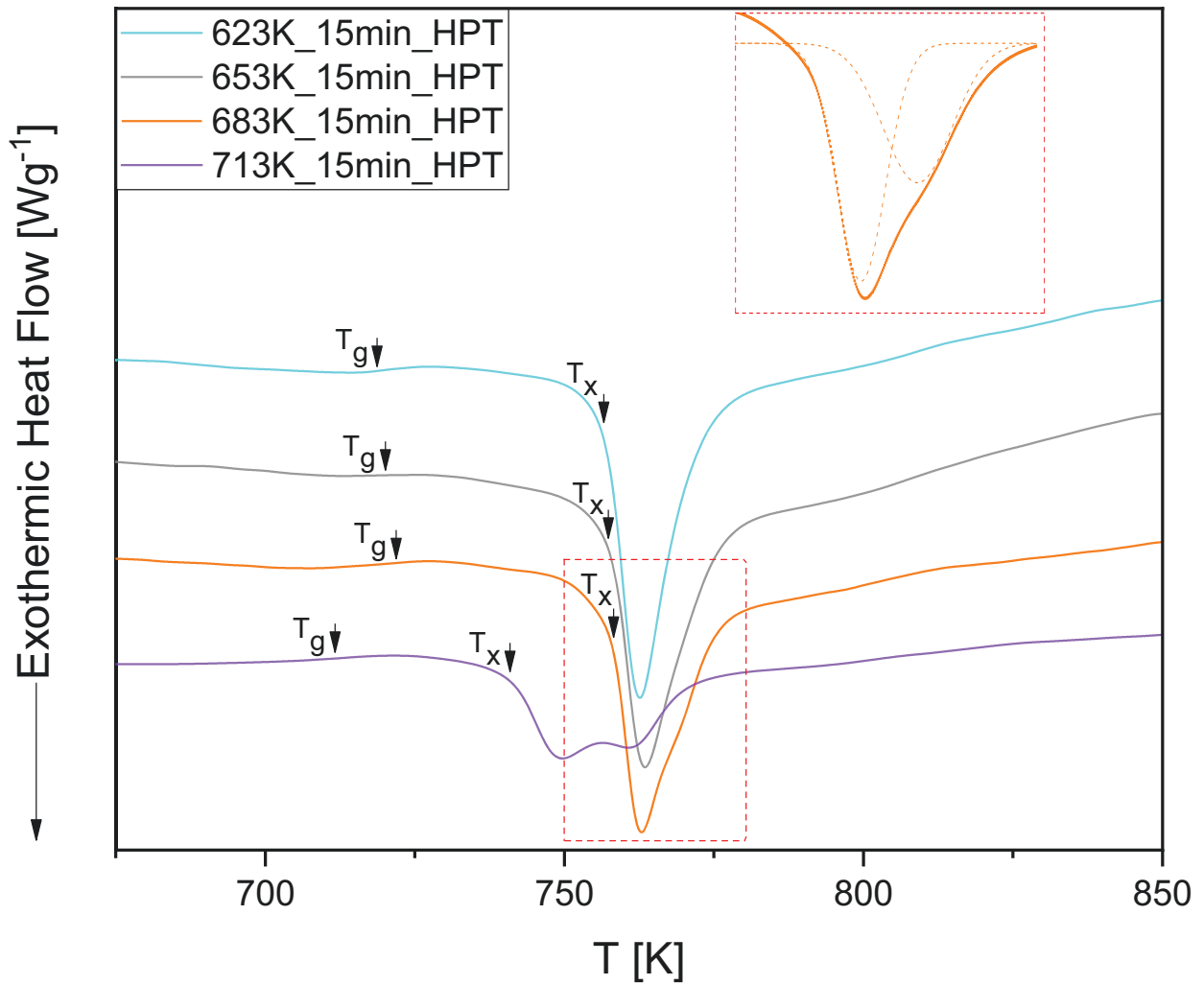


Figure 3.3: Illustration of differential scanning calorimeter curves for Post-HPTed samples with different pre-annealing treatments (623K-15min-HT + HPT, 653K-15min-HT + HPT, 683K-15min-HT + HPT, 713K-15min-HT + HPT(sample 3 - 6)). Modification in crystallization regime of the 683K-15min-HT + HPT deconvoluted into two main peaks is presented clearly in the inset.

The temperature is set constant to 683 K, and by increasing the annealing time to 30 and 60 minutes almost no considerable modification is observed. Moreover, glass transition and crystallization temperatures of samples 7 and 8 are almost the same as for the sample 6.

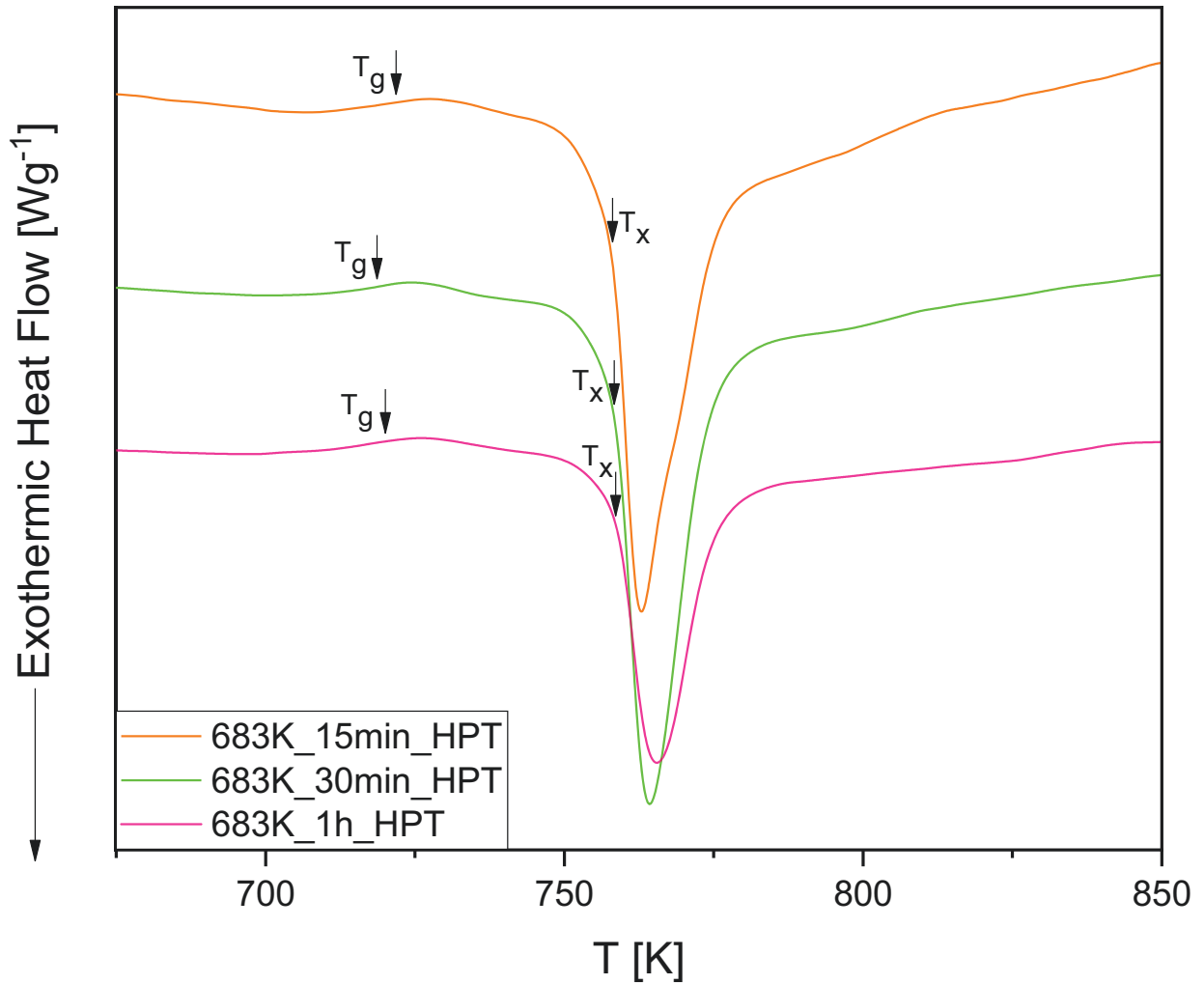


Figure 3.4: DSC data of the samples 5, 7 and 8 (683K-15min-HT + HPT, 683K-30min-HT + HPT, 683K-1h-HT + HPT)

3.4 Influence of Individual and Combinatorial Effect of HPT and HT

By comparing the XRD and DSC data of the samples 3 – 8 the annealing condition for the sample 6 is depicted as the most suitable. Therefore, isothermal heat treatment at 683 K for 15 minutes is decided for the heat treatment. Besides, sample 1 (as-cast) and sample 6 (HT + HPT), sample 2 (HPT), sample 9 (HPT + HT) and sample 10 (HT) were investigated to complete the full set.

The final 5 samples were first studied in the XRD and the results are plotted in the Figure 3.5.

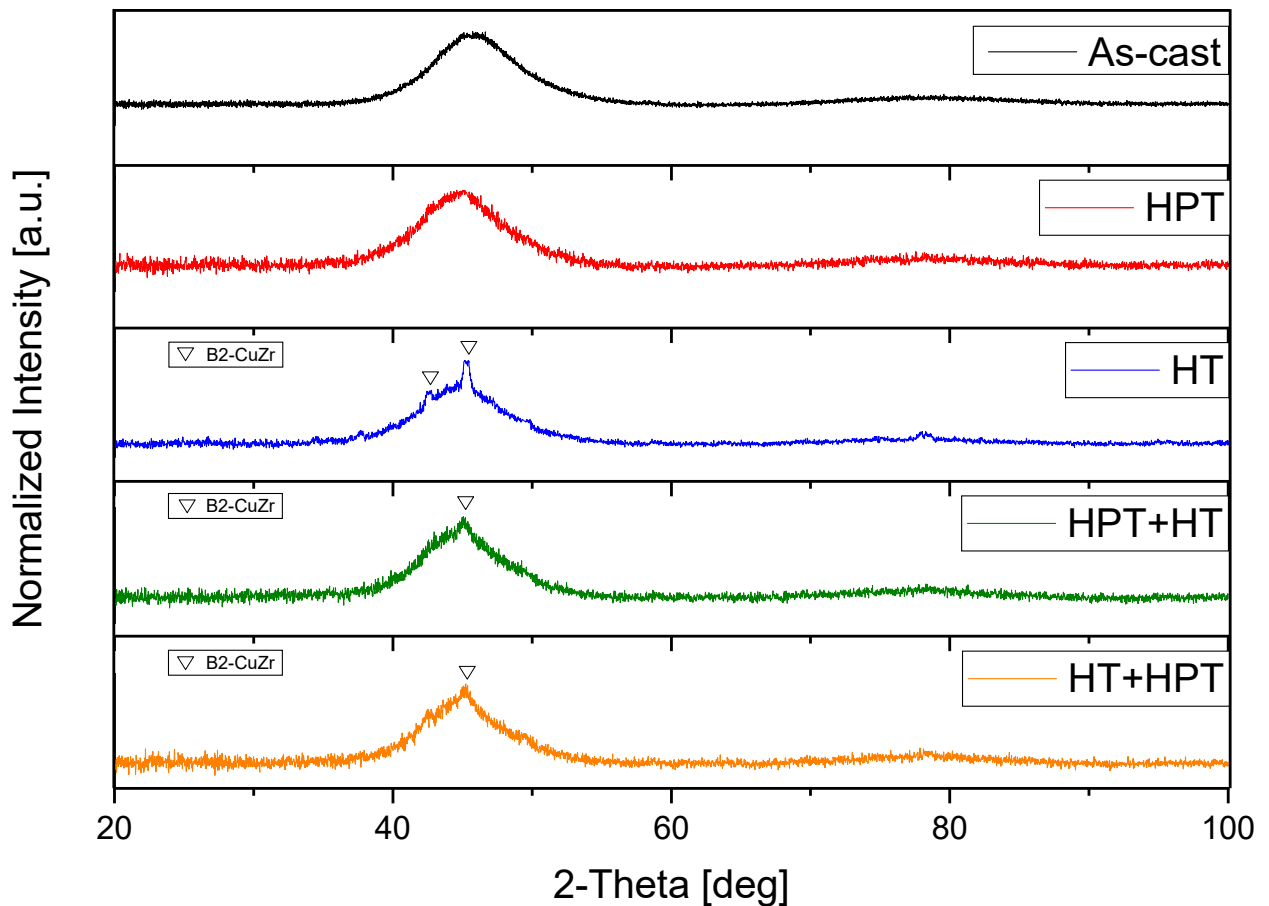


Figure 3.5: The corresponding XRD patterns of the samples (as-cast, HPT, HT, HPT+HT and HT+HPT)

From the XRD no crystalline peak is observed neither for the as-cast nor for the HPT deformed sample as expected. Possible crystals stemming from casting and/or heat treatment can be dissolved through severe shear strain applied during the HPT process. For HT sample one weak crystalline diffraction peak corresponding to a mixture crystalline structure consisting of $\text{Cu}_{10}\text{Zr}_7$ and CuZr_2 and one another clear-cut peak from B2-CuZr phase are superimposed on the broad amorphous scattering maxima. One single crystalline peak is emerged in the broad diffraction pattern of HPT+HT and HT+HPT samples, and this peak is an index to the precipitation of B2-CuZr phase, which is more pronounced for HT+HPT.

Considering HT sample in reference to as-cast, as Cu-rich and Zr-rich zones, precipitated from $\text{Cu}_{10}\text{Zr}_7$ and CuZr_2 , requires a long range redistribution of atoms below the eutectoid transformation temperature (T_E) to form Cu-rich and Zr-rich regions [66]. Continuous cooling transformation diagram (CCT) of CuZr-based alloy illustrated in figure 3.6 indicates that the melt from above T_L can be casted to glass by two different critical cooling rates, R_C and R_{B_2} , corresponding to formation of the largest monolithic BMG and the largest BMGC with a single B2-CuZr phase respectively. As the cooling rate is kept lower than R_{B_2} the metastable

B2 phase is transformed to eutectoid phases below T_E [67]. The casted BMG is heat treated next to achieve structural configuration with nucleation crystallization in nano scale, by which B2-CuZr phase is precipitated in the lower temperature range due to composition similarity of equiatomic CuZr intermetallic compound to the glassy phase [68], since long range distribution of Cu and Zr at the sub- T_g annealing Temperature (T_a) is barely possible (low atomic mobility).

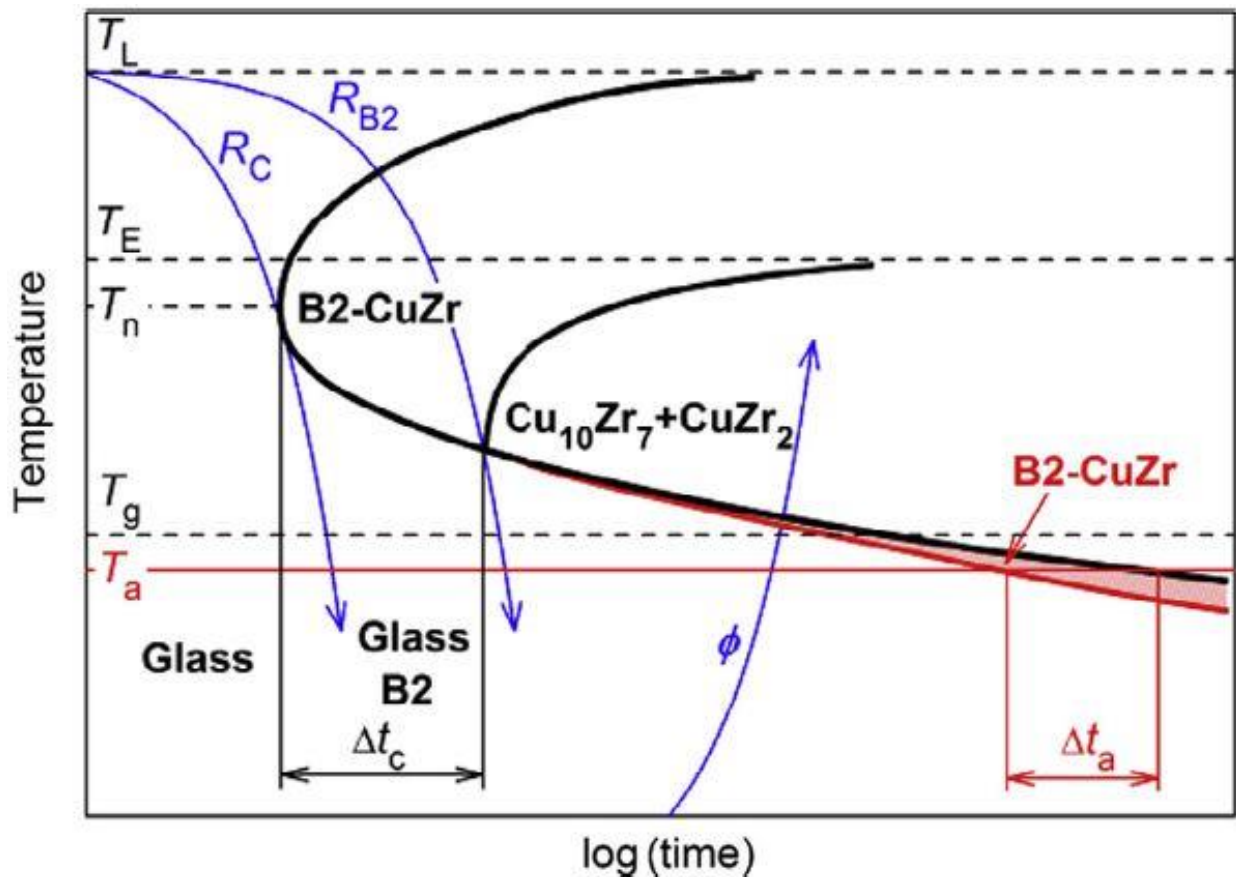


Figure 3.6: CCT schematic of CuZr-based alloy during casting. Red curve shows primary precipitation of B2-CuZr phase during heat treatment at onset of T_a . Δt_c is time window to form BMGC with single B2 and Δt_a is time window to form B2 phase in the precursory glass by heating rate ϕ – adapted from [69].

The samples were afterwards investigated in DSC and are summarized in table 3.3 together with their thermal data.

Table 3.3: Samples exposed to different post-treatment.

Samples	T_g (K)	T_x (K)	ΔT	ΔH_x (J/g)
1. As-cast	718,6	756,7	38,1	39
2. HPT	722,4	757,3	34,9	38,6
3. HT	718,1	753,4	35,3	42,3
4. HPT + HT	719,5	755,4	35,9	58,5
5. HT + HPT	722,1	757,2	35,1	72,1

To cast the largest possible BMG, the cooling rate was kept at its threshold during suction casting, therefore according to the DSC curves of as-cast and HPT samples between the dash lines shown in Figure 3.7 first after homogenization of microstructure via HPT process the ideal glass is achieved. The width of the supercooled liquid region (SCLR), determined by the difference between T_x and T_g , is decreased for HPT sample compared to that of the as-cast due to shift of T_g to higher temperature, in line with findings in the literature [70]. Increase in the T_g after HPT implies that a more stable glass is achieved. SCLR is a parameter to reflect the formability of BMGs of similar chemical composition [70]. For HT sample substantial drop in T_x is observed showing the thermal stability decrease of the glassy phase. For HPT+HT ΔT became larger with the shift of T_g to lower temperature compared to the HPT sample revealing that the structural disordering due to HPT is partially suppressed by post-annealing. Over that for HPT+HT and HT+HPT a broadening in the crystallization peak and thus substantial rise in ΔH_x (crystallization enthalpy) is observed due to the shoulder given to the exothermic peak on the left side. Exothermic peaks in the continuous DSC curves of CuZr-based metallic glasses regardless of Al-quantity correspond to transformation of glass to eutectoid phases [71].

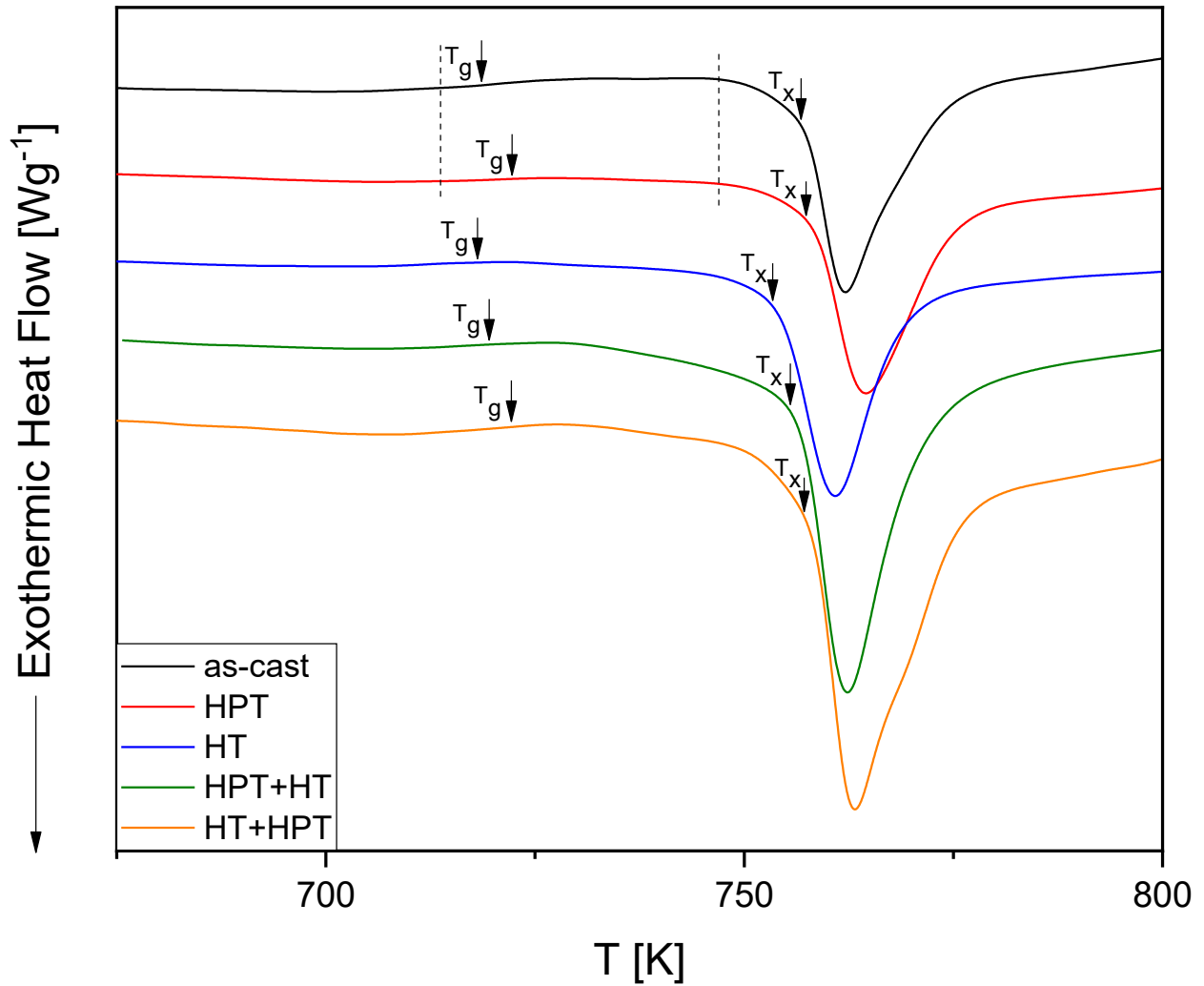


Figure 3.7: Comparison of differential scanning calorimeter curves for as-cast, HPT, HT, HPT + HT, HT + HPT samples

Microhardness profiles of the samples are shown in figure 3.8. The Vickers Hardness is measured with a load of 1000 g. Variation in hardness acquired from as-cast sample can be ascribed to the compositional segregation associated with cooling rate gradient during casting. Tremendous softening due to volumetric dilatation is observed for HPTed samples from the center to the edge, as the applied shear strain and plastic flow induced by HPT increase with radius. Regarding viscosity, CuZr-based alloy systems show deviation from Arrhenius behavior at sub- T_g temperature, and even short-time sub- T_g annealing can cause structural reordering or phase decomposition [55, 72]. Substantial increase is observed in hardness values for HT sample. Compared to the as-cast sample, HPT causes an average hardness decrease of almost 20 HV, whereas HT leads to an average hardness increase of almost 20 HV. For HT sample This increase in hardness can be linked to an increased B2-CuZr fraction volume in correspondence with the formation of hard intermetallic compounds after partial crystallization through annealing [53, 54]. The hardening tendency with increasing the B2-CuZr fraction volume can be originated through the formation of the

nano-scale size of B2-CuZr and the structural relaxation of the glassy matrix. The average hardness value for the HPT+HT sample depicted in table 3.4 is lower than that of the HT+HPT sample. Furthermore, HPT+HT sample exhibits an even hardness profile along the radius revealing the behavior of HPT+HT sample is rather influenced by HT than HPT in comparison, whereas on HT+HPT sample the effect of HPT is dominating. To summarize, HPT + HT treated sample exhibits a homogenous hardness profile with relatively high Vickers hardness across the sample.

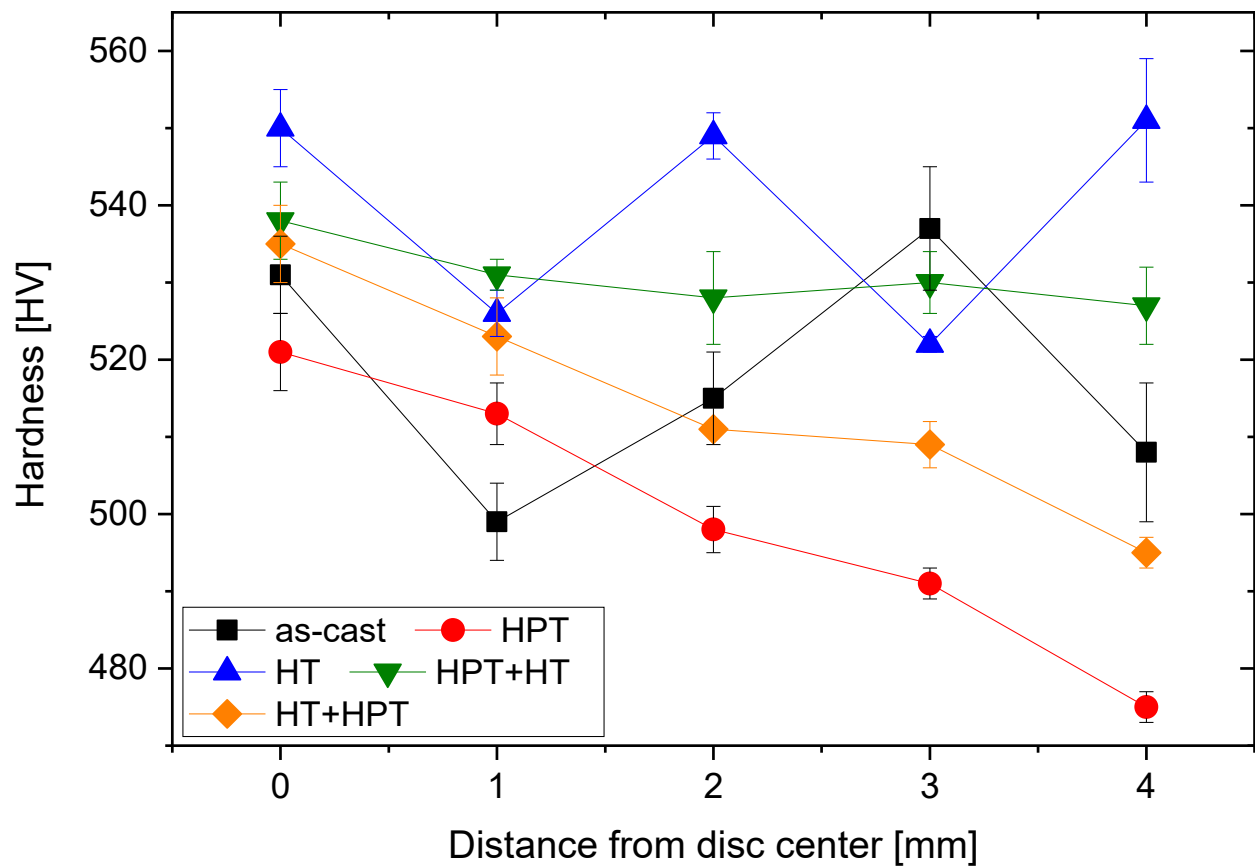


Figure 3.8: Microhardness profiles as a function of the distance from the disc center for the as-cast, HPT, HT, HPT+HT and HT+HPT samples. The measurements are performed at room temperature with a maximum load of 1000 g.

Table 3.4: Average hardness values together with standard deviation of measurements for as-cast, HPT, HT, HPT+HT and HT+HPT samples.

As-cast	HPT	HT	HPT+HT	HT+HPT
518 ± 16	499 ± 18	539 ± 16	531 ± 4	514 ± 15

Figure 3.9 shows the dynamic mechanical analysis of 5 different samples being investigated under 3-point bending. The as-cast sate sample shows an increase in the storage modulus (E') from 88 GPa to 105 GPa as the material enters to the α relaxation region. The HPT treatment leads to a drastic drop in E' (from 88 GPa to 72 GPa) within the same relaxation region, indicating a clear rejuvenation. On the contrary, the HT treatment leads to a shift of the hump observed for the as-cast sample towards higher temperatures, indicating the annihilation of free volume. The HT+HPT sample displays a similar behavior to the only-HPTed sample with a gradual decrease in E' above 600 K as it enters to the structural relaxation region. The vice-versa treatment, HPT+HT leads to a more stabilized E' till higher temperatures (up to 700 K). Thus, HPT+HT treatment leads to an increase in the thermal and structural stability of 100 K. Stiffening behavior of elastic modulus is observed for the HT+HPT sample at the onset of glass transition [73].

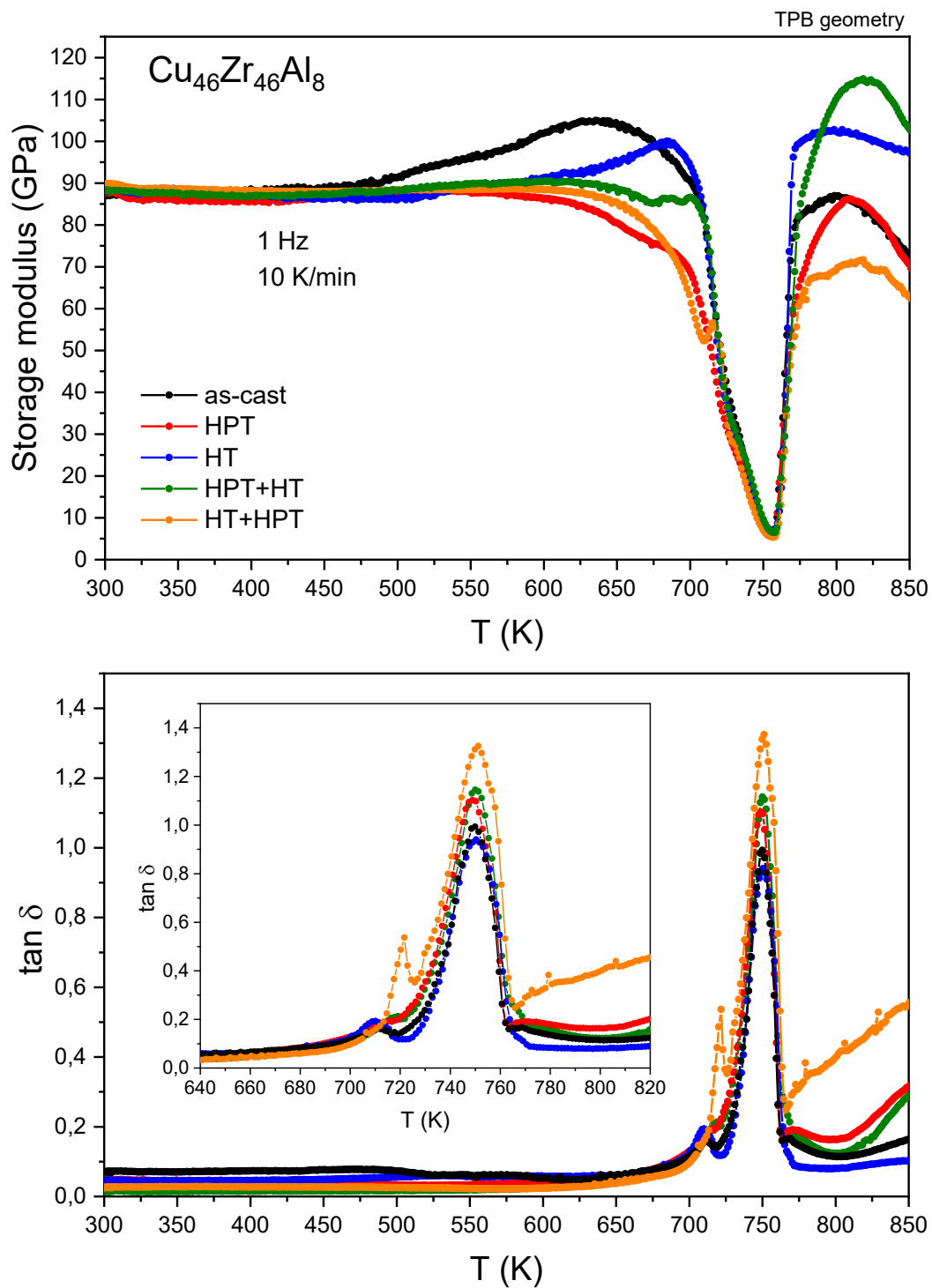


Figure 3.9: DMA Analysis of 5 different samples. (top) storage modulus (below) loss modulus profiles as a function of temperature.

Figure 3.10 illustrates the dilatometer measurement. The influence of HPT (red curve) on the structural relaxation region, observed by DMA, is also reflected on this static measurement. The slope of the as-cast and HT samples changes only after 650 K which is close to its T_g . A pronounced thermal contraction $\Delta L/L_0$ is observed as the material is heated up to 600 K owing to the change in viscosity. On the contrary, no stiffening effect is observed around T_g for the HT and as-cast samples, pointing out that the static mode type of measurement is less sensitive to structural changes around the glass transition temperature.

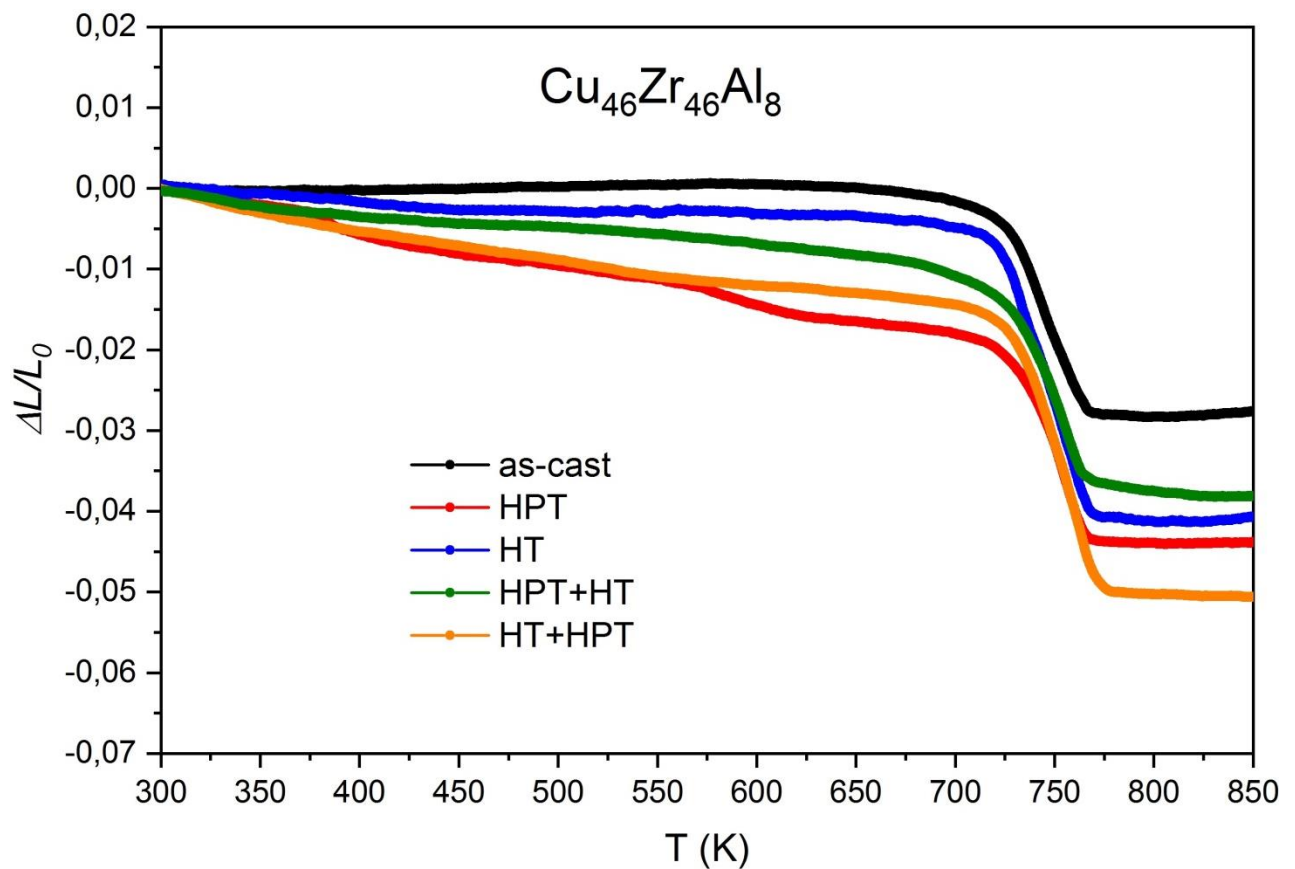


Figure 3.10: Thermal expansion data of the samples as-cast, HPT, HT, HPT+HT and HT+HPT

SEM micrographs of the samples as-cast, HPT, HT, HPT+HT and HT+HPT are shown in figures 3.11 – 3.15, respectively, as follows.

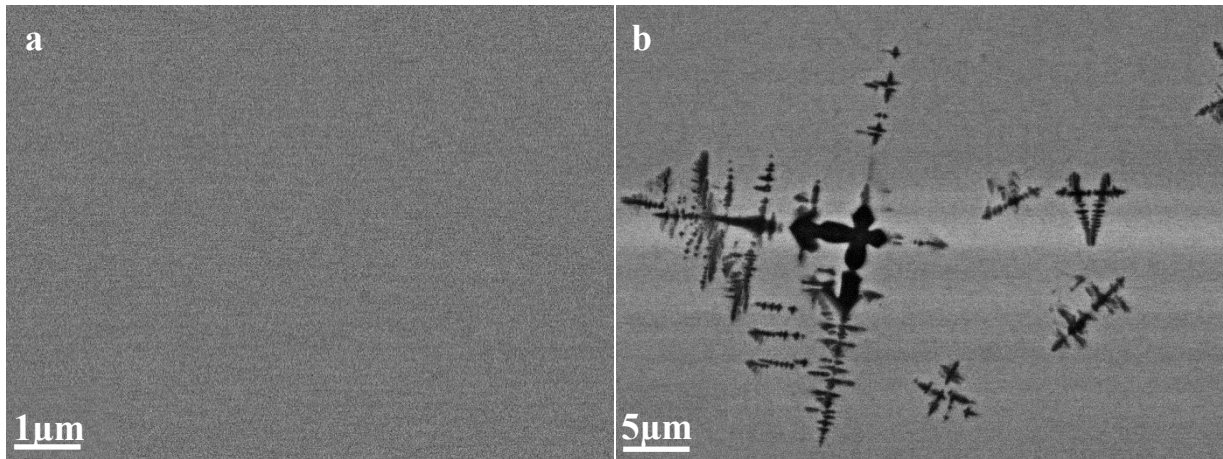


Figure 3.11: SEM images of the as-cast sample. (a) Neither crystals nor any features (i.e. voids, shear bands) in the structure confirming that the as-cast sample is amorphous. (b) However few crystals are observed. The crystals are in the shape of dendrites.

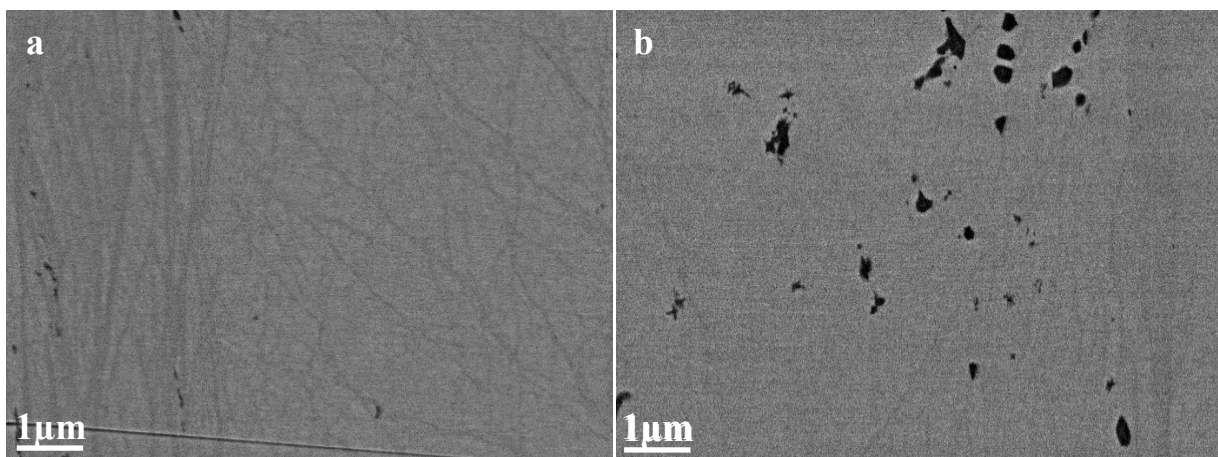


Figure 3.12: SEM images of the HPT sample looking into cross section. (a) Nearly no crystal is observed throughout the structure of the HPT sample. (b) Very few crystals are observed primarily at the center. The crystals are either irregular or round. Besides shear bands are developed due to severe deformation during HPT process.

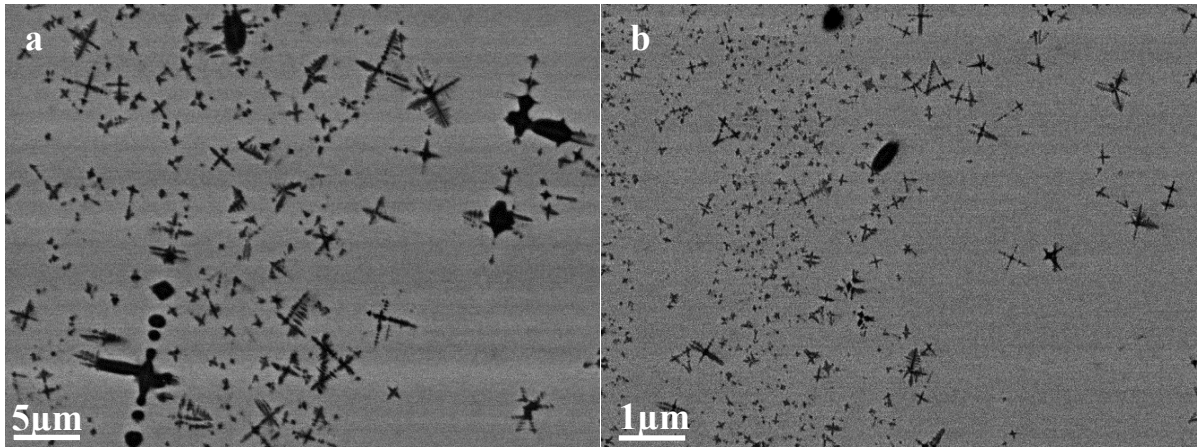


Figure 3.13: SEM micrographs of the HT sample, (a) and (b). Dendritic and irregular-form crystals are created during annealing. Dendritic crystals can be formed upon heat treatment.

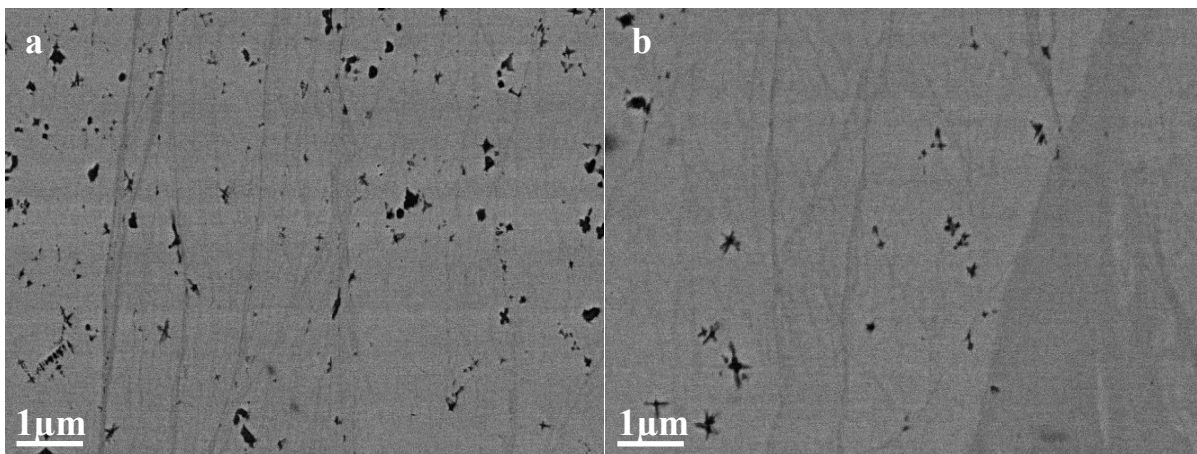


Figure 3.14: The cross-sectional SEM images of the HPT+HT sample in (a) and (b). The crystals are non-uniform but homogenously dispersed. Many shear bands are observed in all parts of the examined sample. By comparing HPT+HT to just-HT sample, it can be concluded that pre-HPT increases the resistance of the material to crystallization.

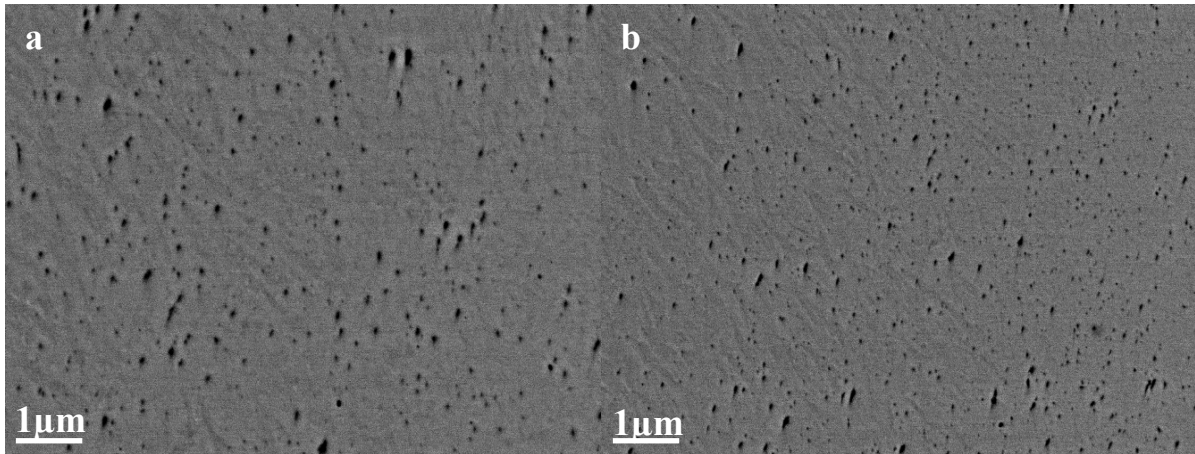


Figure 3.15: SEM images of the HT+HPT sample in (a) and (b). The crystals are rather round and homogenously dispersed.

Figure 3.16 shows the region investigated for the SEM-EDX line scan analysis. The dendritic and irregular particles are rich in Al and Zr at the expense of Cu. EDX mapping also confirms this result (figure 3.17), for the darker second phase regions the corresponding turquoise color indicates the combination of Al- and Zr- elements. The BMG matrix has a random mixture of these elements, confirming the amorphous nature. Table 3.5 depicts the compositional analysis of the investigated region. The matrix composition is similar to the nominal composition of $\text{Cu}_{46}\text{Zr}_{46}\text{Al}_8$ in atomic percentage determined from scaling of the raw elements before casting. However, for the second phase regions, there is a pronounced increase in Zr (by 3 at. %) and Al (by 7 at. %) at the expense of Cu content.

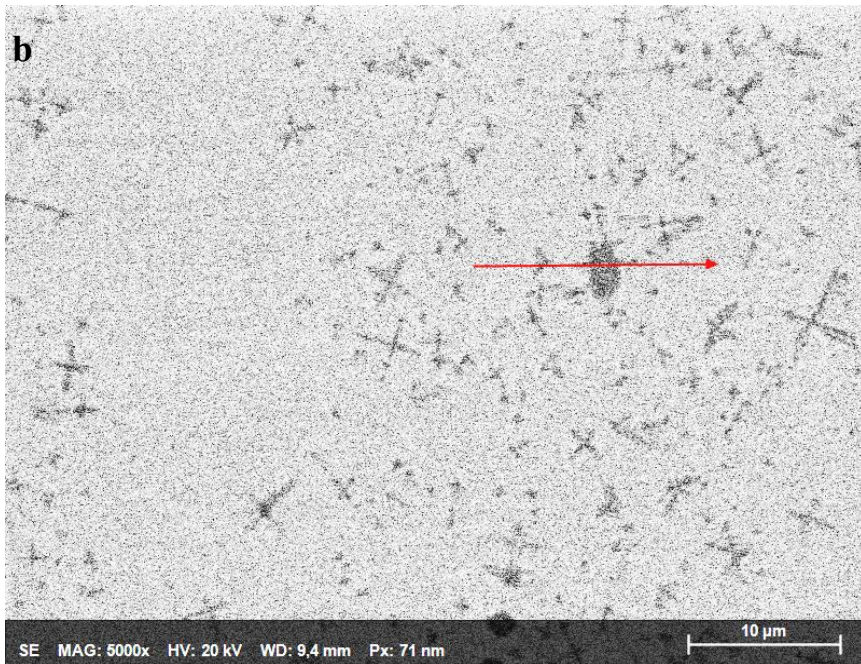
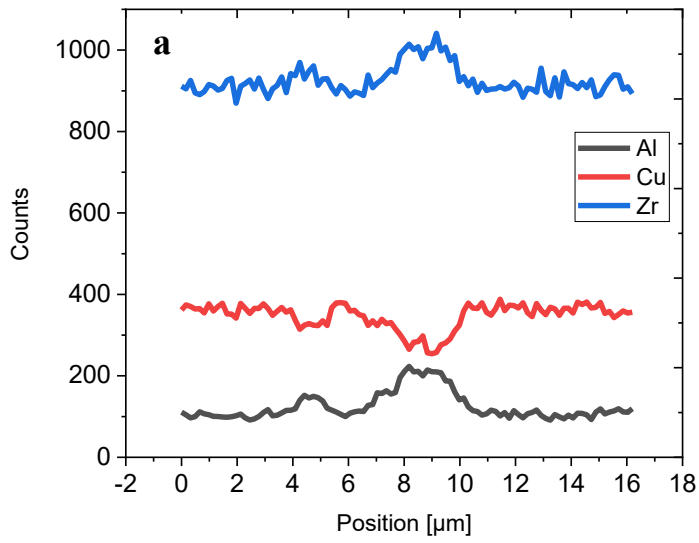


Figure 3.16: (a) Energy dispersive X-ray (EDX) profile of the Cu, Zr and Al in terms of scan position and (b) the corresponding line scan. The dendritic and irregular particles are rich in Al and Zr at the expense of Cu.

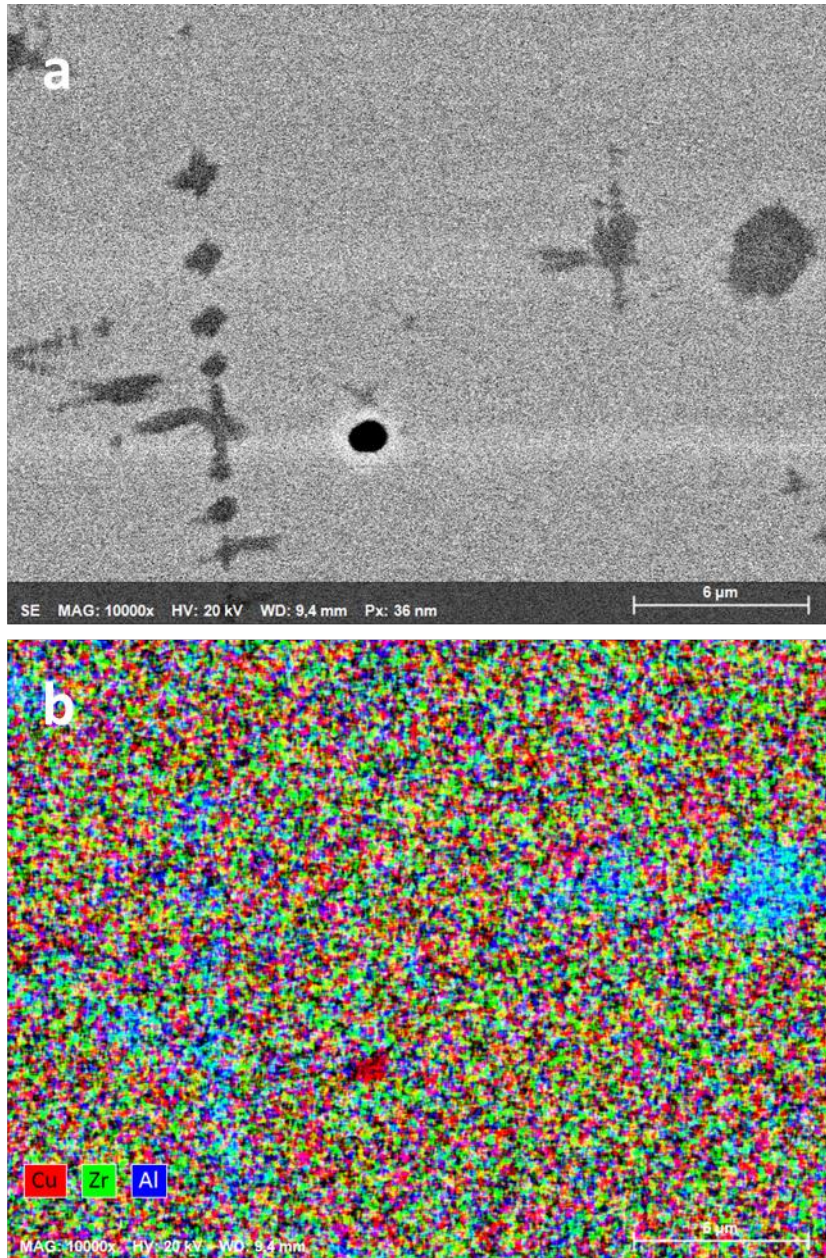


Figure 3.17: (a) SEM image of an as-cast sample (magnification 10000X) containing dendrites and void. (b) EDX mapping of the corresponding region. The dendritic regions are Al- and Zr-rich.

Table 3.5: Composition analysis of the region in Figure 3.17.

	Al	Cu	Zr
Matrix	7,54	45,38	47,17
S.D.	0,15	0,49	0,38
Dendrite	14,59	35,24	50,16
S.D.	0,92	1,63	0,73

The as-cast sample is indeed amorphous, confirmed by TEM investigation (figure 3.18). In some regions, very few crystals are observed (figure 3.19).

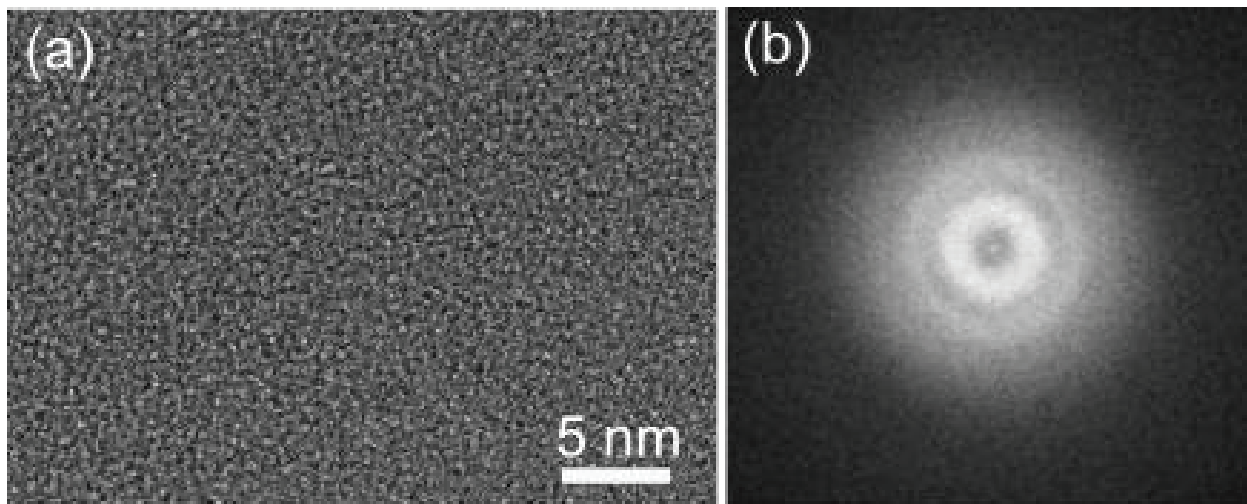


Figure 3.18: (a) HRTEM of the as-cast sample showing amorphous structure and (b) the corresponding Fast Fourier Transform (FFT).

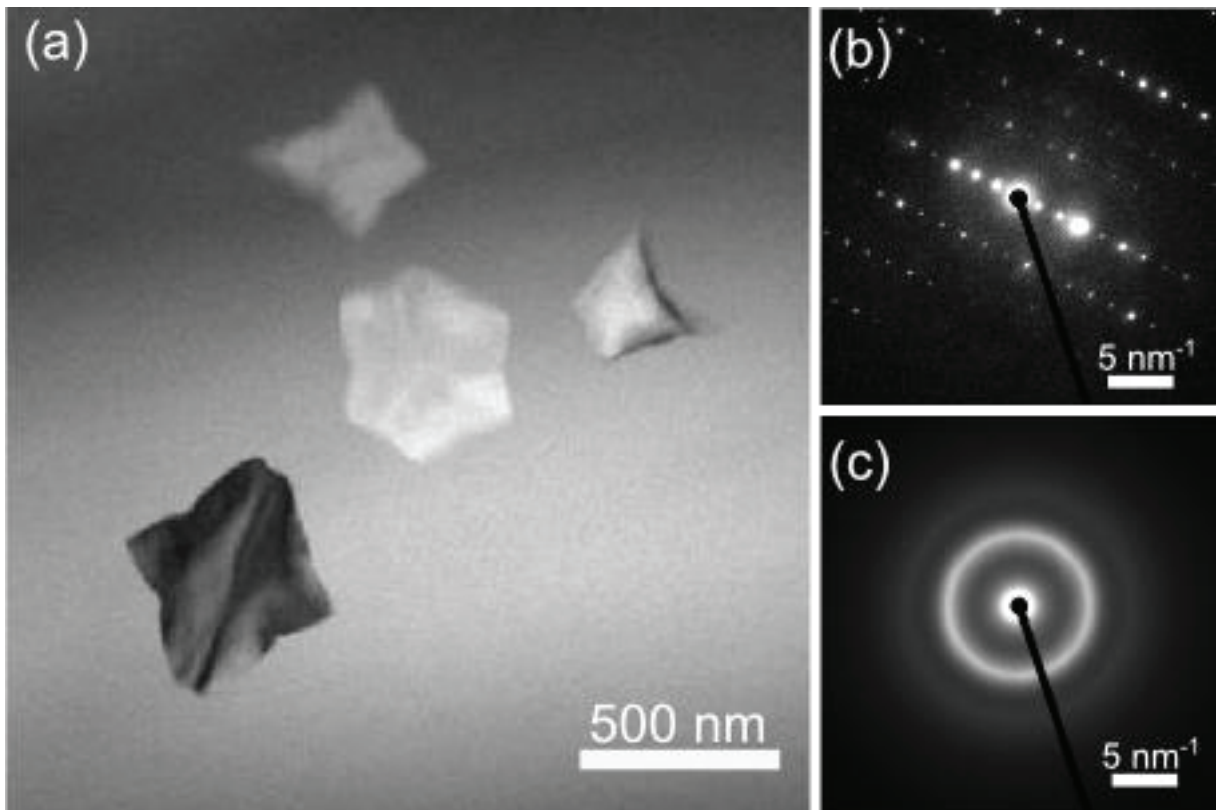


Figure 3.19: Bright Field (BF) image shows the crystals in the amorphous matrix of the as-cast sample (a). The diffraction patterns of oriented crystals and the matrix are given in (b) and (c), respectively.

The HPT sample is amorphous, confirmed by TEM investigation (figure 3.20). However, similar to the as-cast sample, it contains crystals in very few areas. These crystals are heavily deformed and broken into fragments (figure 3.21).

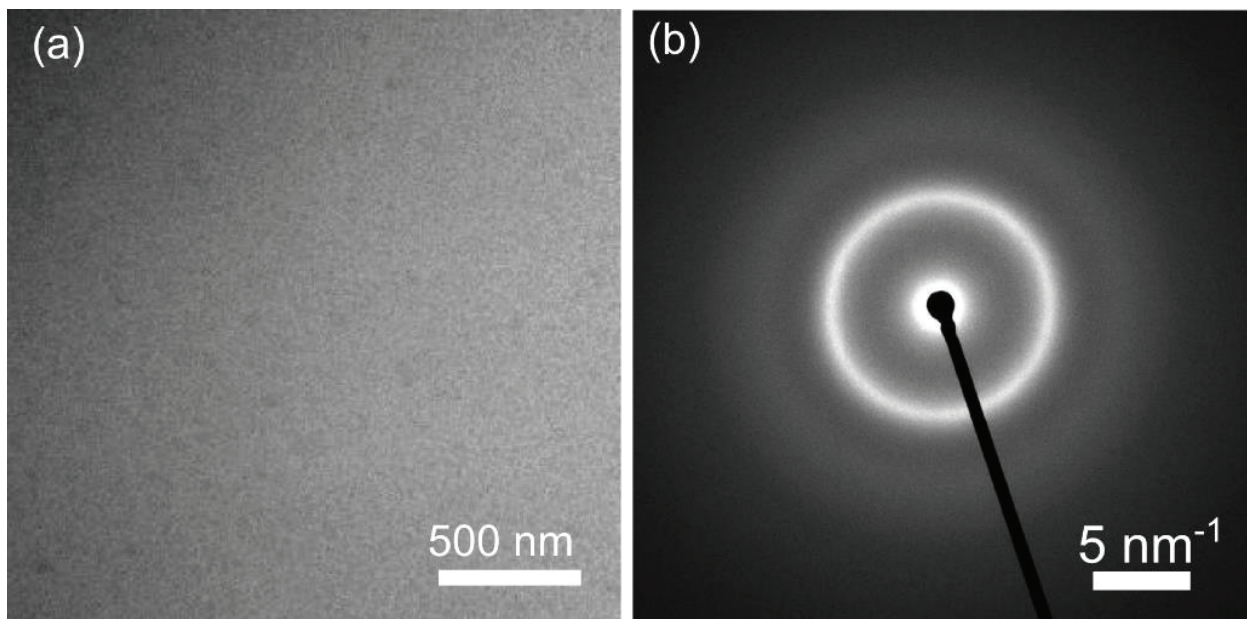


Figure 3.20: BF image (a) and corresponding diffraction pattern (b) of the HPT sample indicate that the sample is amorphous.

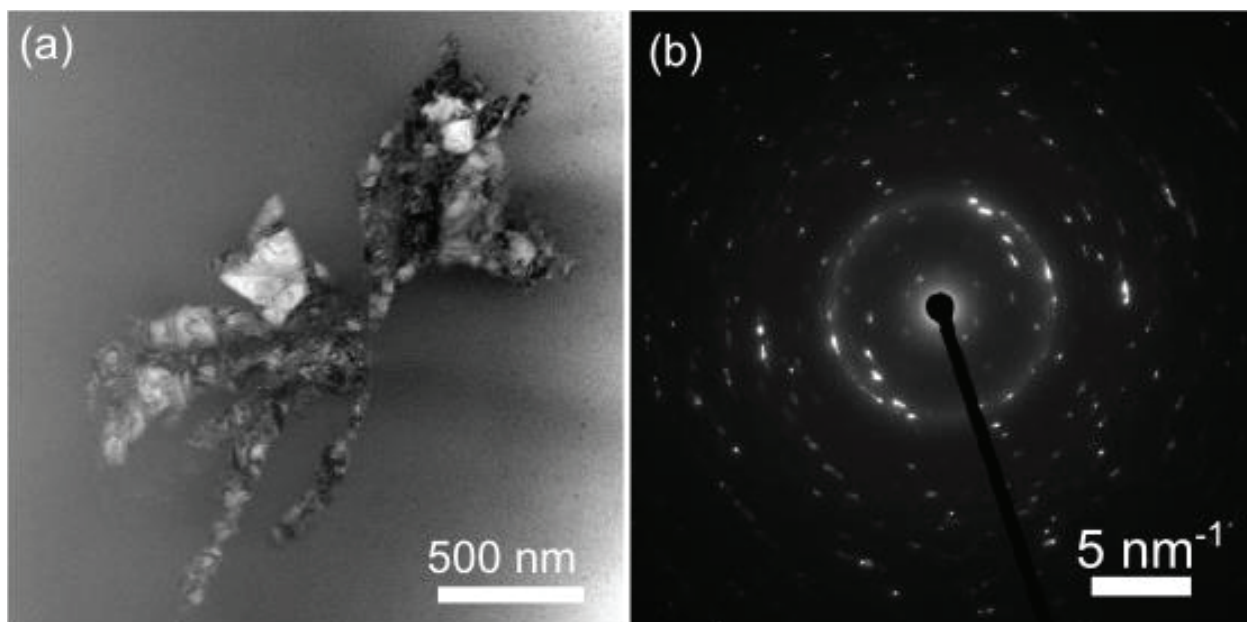


Figure 3.21: BF image (a) and corresponding diffraction pattern (b) of the HPT sample show a deformed crystal in the amorphous matrix. No clear orientation of crystals is observed.

HT sample contains crystals, detected by TEM investigation (figure 3.22).

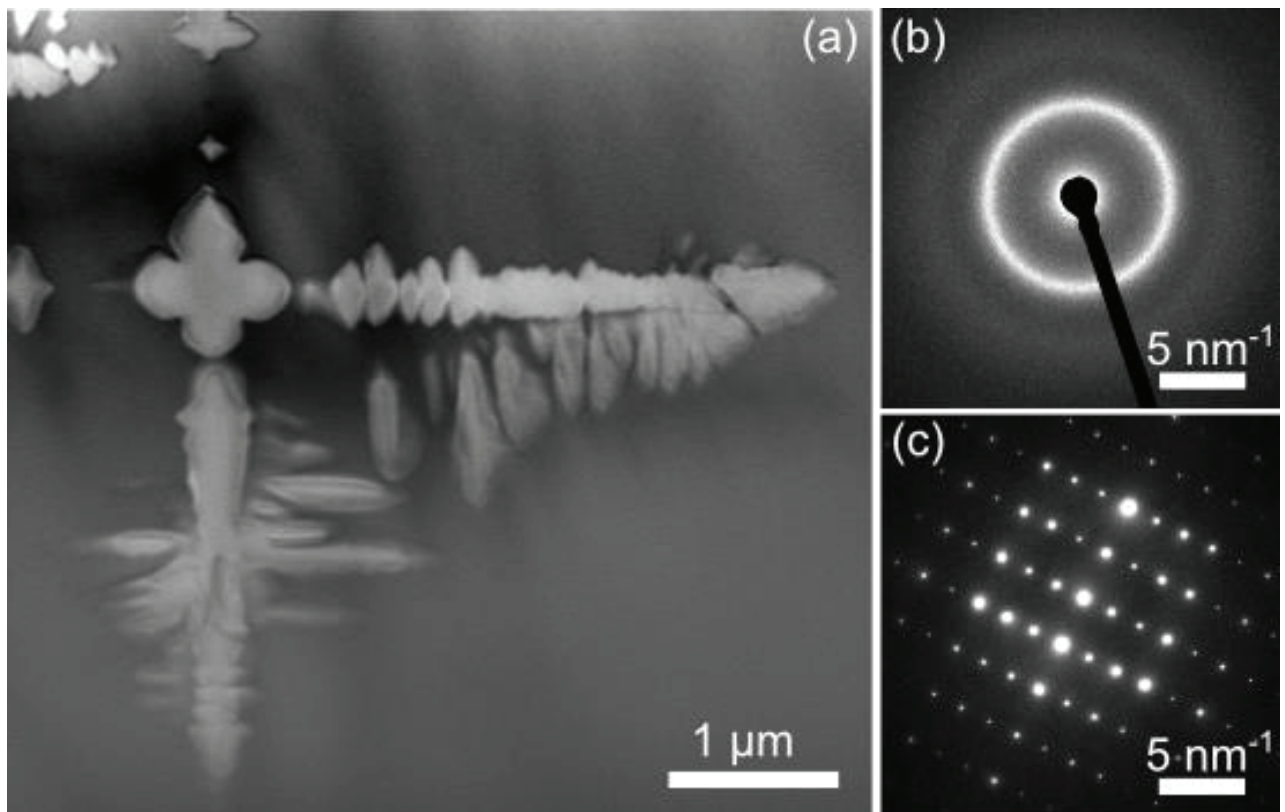


Figure 3.22: (a) BF image shows crystals in the amorphous matrix of the HT sample. The diffraction patterns of the matrix and a crystal are given in (b) and (c), respectively.

TEM micrograph of the HPT+HT sample is similar to the HT sample.

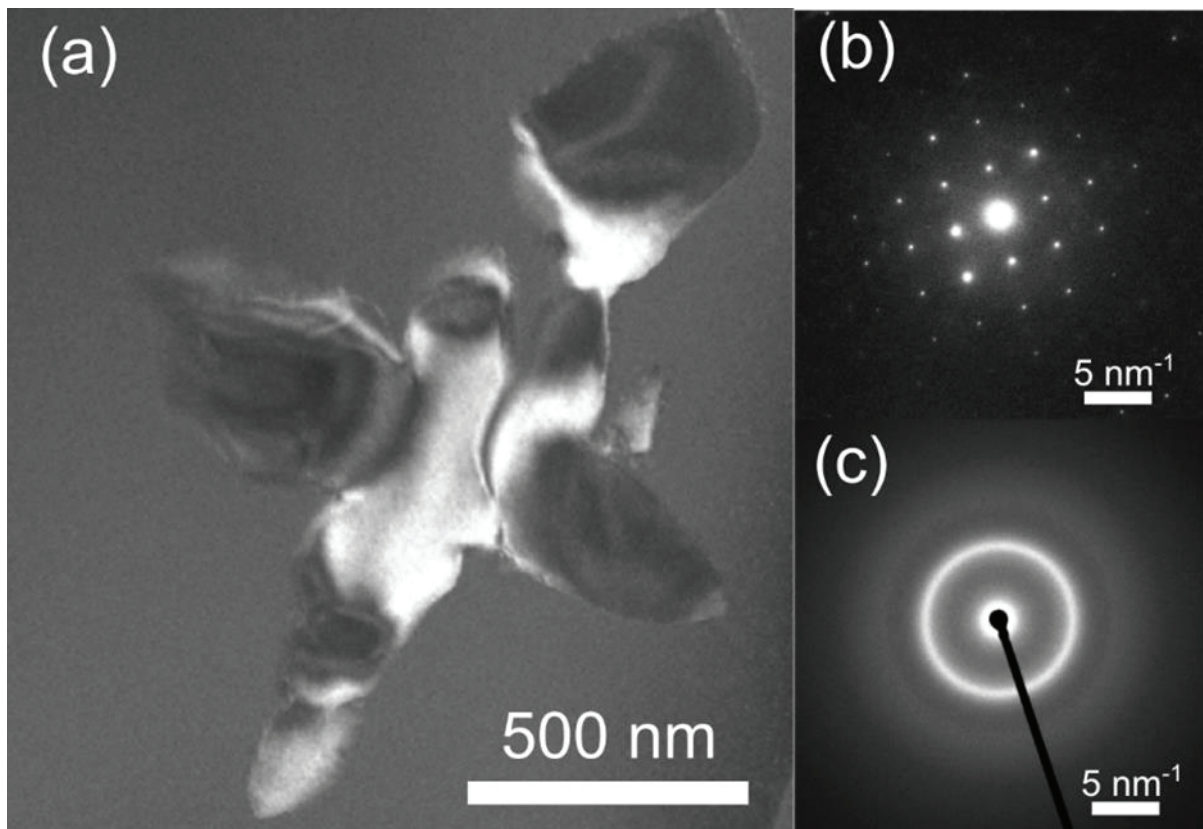


Figure 3.23: (a) DF image displaying crystals in the amorphous matrix of the HPT+HT sample. The diffraction patterns of the crystal and the amorphous matrix are given in (b) and (c), respectively.

BF images of the HT+HPT sample corroborates the findings from the SEM images, where the majority of crystals becomes rounder upon HPT treatment.

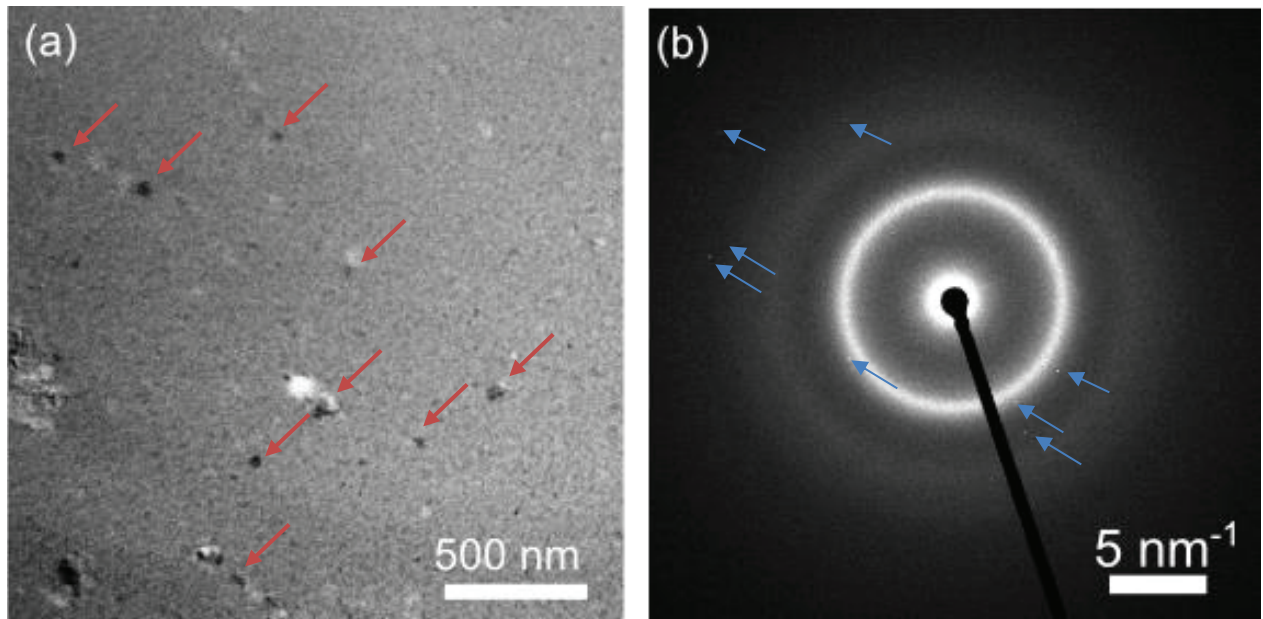


Figure 3.24: (a) BF image shows fragmented crystals in the amorphous matrix of the HPT+HT sample. (b) The corresponding diffraction pattern shows an amorphous halo with some crystalline reflections.

Chapter 4 - General Conclusion and Outlook

This study shows the changes in the mechanical, thermal and structural properties of a CuZr-based bulk metallic glass (BMG) with a nominal composition of $\text{Cu}_{46}\text{Zr}_{46}\text{Al}_8$ upon severe plastic deformation (SPD) and sub- T_g heat treatment (HT) separately and alternately. SPD of $\text{Cu}_{46}\text{Zr}_{46}\text{Al}_8$ BMG via high pressure torsion (HPT) causes an increase in the amount of free volume (i.e., dilatation) and formation of nanoclusters. Conversely, sub- T_g annealing of $\text{Cu}_{46}\text{Zr}_{46}\text{Al}_8$ BMG leads to the reduction of free volume (i.e., densification) in companion with the fluctuation in the chemical ordering. Despite the local temperature rise during HPT (close to glass transition), induced modifications in the microstructure after deformation are mainly ascribed to high extent of applied shear strains which overcome thermal effects. By comparing the experimental results of the differently treated samples (i.e., as-cast, HPT, HT, HPT+HT and HT+HPT) main findings can be summarized in the following:

- Casting a plate (40 mm in diameter and a 2 mm in thickness) can generate a TEM-amorphous metallic glass. Post-sample preparation and HPT process do not alter this amorphous nature.
- At the early stage of sub- T_g annealing, primarily a metastable B2-CuZr phase in nano to micrometer-scale precipitates. By further increasing the annealing time, a eutectoid reaction from the B2 phase to low temperature equilibrium phases, $\text{Cu}_{10}\text{Zr}_7$ and CuZr_2 , occurs. Besides, pre-HPT escalates the resistance of the material against crystallization, whereas through post-HPT homogeneously dispersed crystals can be reached.
- A large fluctuation in hardness profile of the as-cast and HT samples is observed. Via controlled post-HT of the HPTed sample an even hardness profile with a relatively higher Vickers hardness across the BMG matrix can be achieved.
- According to thermomechanical analysis, the HPT+HT treated BMG is a more stable glass, as the low-temperature shoulder on the crystallization peak disappears. Bulk metallic glass composite (BMGC) with uniformly dispersed crystals in sizes of nano to micro-scale is found to be beneficial for the enhancement of strength retention at temperatures close to glass transition. Further, DMA shows a higher drop in viscosity of the HT+HPT treated BMG.
- By taking an alternate order of treatments (first HT followed by HPT) we can achieve uniform distribution of the crystals based on the SEM findings. Al- and Zr-rich second phase shows remarkable compositional difference compared to the matrix phase confirmed by the EDX attached to SEM.

- Both HPT+HT and HT+HPT treated BMGs show enhanced microstructural and thermomechanical properties compared to as-cast, just HPTed or just HTed samples.

In conclusion, combinatorial two-stage treatment of thermal annealing and plastic deformation is a promising approach to enhance the mechanical properties of bulk metallic glasses.

References

- [1] C.A. Schuh, T.C. Hufnagel, U. Ramamurty, Overview No.144 - Mechanical behavior of amorphous alloys, *Acta Mater.* 55(12) (2007) 4067-4109.
- [2] C. Suryanarayana, A. Inoue, Iron-based bulk metallic glasses, *Int. Mater. Rev.* 58(3) (2013) 131-166.
- [3] W.H. Wang, C. Dong, C.H. Shek, Bulk metallic glasses, *Mater. Sci. Eng., R* 44(2-3) (2004) 45-89.
- [4] J. Schroers, The superplastic forming of bulk metallic glasses, *JOM* 57(5) (2005) 35-39.
- [5] W.L. Johnson, Bulk amorphous metal - An emerging engineering material, *JOM* 54(3) (2002) 40-43.
- [6] M. Telford, The case for bulk metallic glass, *Mater. Today* 7(3) (2004) 36-43.
- [7] M.F. Ashby, A.L. Greer, Metallic glasses as structural materials, *Scr. Mater.* 54(3) (2006) 321-326.
- [8] M.W. Chen, A brief overview of bulk metallic glasses, *NPG Asia Mater.* 3 (2011) 82-90.
- [9] J.W. Qiao, H.L. Jia, P.K. Liaw, Metallic glass matrix composites, *Mater. Sci. Eng., R* 100 (2016) 1-69.
- [10] A.L. Greer, Metallic glasses ... on the threshold, *Mater. Today* 12(1-2) (2009) 14.
- [11] X.Q. Liu, Y.G. Zheng, X.C. Chang, W.L. Hou, J.Q. Wang, Influence of HVOF Thermal Spray Process on the Microstructures and Properties of Fe-based Amorphous Nano metallic Coatings, *Mater. Sci. Forum* 633-634 (2010) 685-694.

- [12] H. Zhou, C. Zhang, W. Wang, M. Yasir, L. Liu, Microstructure and Mechanical Properties of Fe-based Amorphous Composite Coatings Reinforced by Stainless Steel Powders, *J. Mater. Sci. Technol.* 31(1) (2015) 43-47.
- [13] N. Nishiyama, K. Amiya, A. Inoue, Novel applications of bulk metallic glass for industrial products, *J. Non-Cryst. Solids* 353(32-40) (2007) 3615-3621.
- [14] H. Wu, X.D. Lan, Y. Liu, F. Li, W.D. Zhang, Z.J. Chen, X.F. Zai, H. Zeng, Fabrication, tribological and corrosion behaviors of detonation gun sprayed Fe-based metallic glass coating, *Trans. Nonferrous Met. Soc. China* 26(6) (2016) 1629-1637.
- [15] L. Zhang, H. Huang, Micro machining of bulk metallic glasses: a review, *Int. J. Adv. Manuf. Tech.* 100(1-4) (2019) 637-661.
- [16] A.J. Krejcie, S.G. Kapoor, R.E. DeVor, A hybrid process for manufacturing surgical-grade knife blade cutting edges from bulk metallic glass, *J. Manuf. Process.* 14(1) (2012) 26-34.
- [17] B. Sarac, G. Kumar, T. Hodges, S.Y. Ding, A. Desai, J. Schroers, Three-Dimensional Shell Fabrication Using Blow Molding of Bulk Metallic Glass, *J. Microelectromech. Syst.* 20(1) (2011) 1-9.
- [18] B. Sarac, S. Bera, F. Spieckermann, S. Balakin, M. Stoica, M. Calin, J. Eckert, Micropatterning kinetics of different glass-forming systems investigated by thermoplastic net-shaping, *Scr. Mater.* 137 (2017) 127-131.
- [19] M. Hasan, J. Schroers, G. Kumar, Functionalization of Metallic Glasses through Hierarchical Patterning, *Nano Lett.* 15(2) (2015) 963-968.
- [20] J. Schroers, Q. Pham, A. Desai, Thermoplastic forming of bulk metallic glass - A technology for MEMS and microstructure fabrication, *J. Microelectromech. S.* 16(2) (2007) 240-247.

- [21] A.L. Greer, Y.Q. Cheng, E. Ma, Shear bands in metallic glasses, *Mater. Sci. Eng., R* 74(4) (2013) 71-132.
- [22] T. Wada, A. Inoue, A.L. Greer, Enhancement of room-temperature plasticity in a bulk metallic glass by finely dispersed porosity, *Appl. Phys. Lett.* 86(25) (2005).
- [23] D.C. Hofmann, J.Y. Suh, A. Wiest, G. Duan, M.L. Lind, M.D. Demetriou, W.L. Johnson, Designing metallic glass matrix composites with high toughness and tensile ductility, *Nature* 451(7182) (2008) 1085-1090.
- [24] C.A. Volkert, A. Donohue, F. Spaepen, Effect of sample size on deformation in amorphous metals, *J. Appl. Phys.* 103(8) (2008) 083539.
- [25] B. Sarac, J. Schroers, Designing tensile ductility in metallic glasses, *Nat. Commun.* 4 (2013) 2158.
- [26] B. Sarac, Y.P. Ivanov, A. Chuvilin, T. Schöberl, M. Stoica, Z. Zhang, J. Eckert, Origin of large plasticity and multiscale effects in iron-based metallic glasses, *Nat. Commun.* 9(1333) (2018) 1-10.
- [27] B. Sarac, J. Ketkaew, D.O. Popnoe, J. Schroers, Honeycomb Structures of Bulk Metallic Glasses, *Adv. Funct. Mater.* 22(15) (2012) 3161-3169.
- [28] J.J. Lewandowski, W.H. Wang, A.L. Greer, Intrinsic plasticity or brittleness of metallic glasses, *Phil. Mag. Lett.* 85(2) (2005) 77-87.
- [29] K.E. Prasad, U. Ramamurty, Effect of temperature on the plastic zone size and the shear band density in a bulk metallic glass, *Mater. Sci. Eng., A* 535 (2012) 48-52.
- [30] X.K. Xi, D.Q. Zhao, M.X. Pan, W.H. Wang, Y. Wu, J.J. Lewandowski, Fracture of brittle metallic glasses: Brittleness or plasticity, *Phys. Rev. Lett.* 94(12) (2005) 125510.

- [31] J. Schroers, W.L. Johnson, Ductile bulk metallic glass, *Phys. Rev. Lett.* 93(25) (2004) 255506.
- [32] Y.H. Liu, G. Wang, R.J. Wang, D.Q. Zhao, M.X. Pan, W.H. Wang, Super plastic bulk metallic glasses at room temperature, *Science* 315(5817) (2007) 1385-1388.
- [33] W.M. Yang, H.S. Liu, Y.C. Zhao, A. Inoue, K.M. Jiang, J.T. Huo, H.B. Ling, Q. Li, B.L. Shen, Mechanical properties and structural features of novel Fe-based bulk metallic glasses with unprecedented plasticity, *Sci. Rep.* 4(6233) (2014) 1-6.
- [34] K.F. Yao, F. Ruan, Y.Q. Yang, N. Chen, Superductile bulk metallic glass, *Appl. Phys. Lett.* 88(12) (2006) 122106.
- [35] R.D. Conner, W.L. Johnson, N.E. Paton, W.D. Nix, Shear bands and cracking of metallic glass plates in bending, *J. Appl. Phys.* 94(2) (2003) 904-911.
- [36] R.D. Conner, Y. Li, W.D. Nix, W.L. Johnson, Shear band spacing under bending of Zr-based metallic glass plates, *Acta Mater.* 52(8) (2004) 2429-2434.
- [37] C.A. Schuh, A.C. Lund, T.G. Nieh, New regime of homogeneous flow in the deformation map of metallic glasses: elevated temperature nanoindentation experiments and mechanistic modeling, *Acta Mater.* 52(20) (2004) 5879-5891.
- [38] H. Guo, P.F. Yan, Y.B. Wang, J. Tan, Z.F. Zhang, M.L. Sui, E. Ma, Tensile ductility and necking of metallic glass, *Nat. Mater.* 6(10) (2007) 735-739.
- [39] G. Duan, A. Wiest, M.L. Lind, J. Li, W.K. Rhim, W.L. Johnson, Bulk metallic glass with benchmark thermoplastic processability, *Adv. Mater.* 19(23) (2007) 4272-4275.
- [40] J. Schroers, W.L. Johnson, Highly processable bulk metallic glass-forming alloys in the Pt-Co-Ni-Cu-P system, *Appl. Phys. Lett.* 84(18) (2004) 3666-3668.

- [41] B. Zhang, D.Q. Zhao, M.X. Pan, W.H. Wang, A.L. Greer, Amorphous metallic plastic, *Phys. Rev. Lett.* 94(20) (2005).
- [42] J. Schroers, B. Lohwongwatana, W.L. Johnson, A. Peker, Gold based bulk metallic glass, *Appl. Phys. Lett.* 87(6) (2005).
- [43] B. Sarac, D. Söpu, E. Park, J.K. Hufenbach, S. Oswald, M. Stoica, J. Eckert, Mechanical and Structural Investigation of Porous Bulk Metallic Glasses, *Metals* 5(2) (2015) 920-933.
- [44] J. Schroers, T.M. Hodges, G. Kumar, H. Raman, A.J. Barnes, P. Quoc, T.A. Waniuk, Thermoplastic blow molding of metals, *Mater. Today* 14(1-2) (2011) 14-19.
- [45] B. Sarac, *Microstructure-Property Optimization in Metallic Glasses*, Springer International Publishing 2015.
- [46] C. Mangler, C. Rentenberger, I. Humer, L. Reichhart, H.P. Karnthaler, Disordering and reordering of bulk Fe-45at.%Al studied by TEM, *Microsc. Microanal.* 13(S03) (2007) 298-299.
- [47] R. Pippan, S. Scheriau, A. Hohenwarter, M. Hafok, Advantages and limitations of HPT: a review, *Mater. Sci. Forum* 584-586 (2008) 16-21.
- [48] W. Dmowski, Y. Yokoyama, A. Chuang, Y. Ren, M. Umemoto, K. Tsuchiya, A. Inoue, T. Egami, Structural rejuvenation in a bulk metallic glass induced by severe plastic deformation, *Acta Mater.* 58(2) (2010) 429-438.
- [49] J. Qiang, K. Tsuchiya, Composition dependence of mechanically-induced structural rejuvenation in Zr-Cu-Al-Ni metallic glasses, *J. Alloys Compd.* 712 (2017) 250-255.
- [50] L. Krämer, K.S. Kormout, D. Setman, Y. Champion, R. Pippan, Production of Bulk Metallic Glasses by Severe Plastic Deformation, *Metals* 5(2) (2015) 720-729.

- [51] H. Kozachkov, J. Kolodziejska, W.L. Johnson, D.C. Hofmann, Effect of cooling rate on the volume fraction of B2 phases in a CuZrAlCo metallic glass matrix composite, *Intermetallics* 39 (2013) 89-93.
- [52] R. Wei, S. Yang, Y. Chang, Y.F. Li, C.J. Zhang, L. He, Mechanical property degradation of a CuZr-based bulk metallic glass composite induced by sub-T-g annealing, *Mater. Design* 56 (2014) 128-138.
- [53] J.G. Wang, B.W. Choi, T.G. Nieh, C.T. Liu, Crystallization and nanoindentation behavior of a bulk Zr-Al-Ti-Cu-Ni amorphous alloy, *J. Mater. Res.* 15(3) (2000) 798-807.
- [54] H.J. Jun, K.S. Lee, C.P. Kim, Y.W. Chang, Ductility enhancement of a Ti-based bulk metallic glass through annealing treatment below the glass transition temperature, *Intermetallics* 20(1) (2012) 47-54.
- [55] B. Sarac, L. Zhang, K. Kosiba, S. Pauly, M. Stoica, J. Eckert, Towards the Better: Intrinsic Property Amelioration in Bulk Metallic Glasses, *Sci. Rep.* 6 (2016) 1-8.
- [56] B. Sarac, A. Bernasconi, J. Wright, M. Stoica, F. Spieckermann, M. Mühlbacher, J. Keckes, X. Bian, G. Wang, J. Eckert, Structural modifications in sub-Tg annealed CuZr-based metallic glass *Mater. Sci. Eng., A* 707 (2017) 245-252.
- [57] A. Ishii, F. Hori, A. Iwase, Y. Fukumoto, Y. Yokoyama, T.J. Konno, Relaxation of Free Volume in Zr₅₀Cu₄₀Al₁₀ Bulk Metallic Glasses Studied by Positron Annihilation Measurements, *Mater. Trans.* 49(9) (2008) 1975-1978.
- [58] P. Ramasamy, *Soft Ferromagnetic Bulk Metallic Glasses with Enhanced Mechanical Properties*, Technische Universität Dresden, Dresden, 2017.
- [59] B. Sarac, F. Spieckermann, A. Rezvan, C. Gammer, L. Krämer, J.T. Kim, J. Keckes, R. Pippin, J. Eckert, Annealing-assisted high-pressure torsion in Zr₅₅Cu₃₀Al₁₀Ni₅ metallic glass, *J. Alloys Compd.* 784 (2019) 1323-1333.

- [60] Q.P. Cao, J.F. Li, Y.H. Zhou, A. Horsewell, J.Z. Jiang, Free-volume evolution and its temperature dependence during rolling of Cu₆₀Zr₂₀Ti₂₀ bulk metallic glass, *Appl. Phys. Lett.* 87(10) (2005).
- [61] K. Edalati, Y. Hashiguchi, P.H.R. Pereira, Z. Horita, T.G. Langdon, Effect of temperature rise on microstructural evolution during high-pressure torsion, *Mater. Sci. Eng., A* 714 (2018) 167-171.
- [62] M.J. Stefan, Sitzber. Akad. Wiss. Wien. (Abt. II Math. Phys.) (1874) 713-735.
- [63] G.J. Diennes, H.F. Klemm, Theory and Application of the parallel plate plastometer, *J. Appl. Phys.* 17 (1946) 458-471.
- [64] B. Sarac, C. Gammer, L. Deng, E. Park, Y. Yokoyama, M. Stoica, J. Eckert, Elastostatic reversibility in thermally formed bulk metallic glasses: nanobeam diffraction fluctuation electron microscopy, *Nanoscale* 10 (2018) 1081 - 1089.
- [65] J.C. Qiao, J.M. Pelletier, Isochronal and isothermal crystallization in Zr₅₅Cu₃₀Ni₅ Al-10 bulk metallic glass, *Trans. Nonferrous Met. Soc. China* 22(3) (2012) 577-584.
- [66] Y. Wu, H. Wang, H.H. Wu, Z.Y. Zhang, X.D. Hui, G.L. Chen, D. Ma, X.L. Wang, Z.P. Lu, Formation of Cu-Zr-Al bulk metallic glass composites with improved tensile properties, *Acta Mater.* 59(8) (2011) 2928-2936.
- [67] K.K. Song, S. Pauly, Y. Zhang, P. Gargarella, R. Li, N.S. Barekar, U. Kuhn, M. Stoica, J. Eckert, Strategy for pinpointing the formation of B2 CuZr in metastable CuZr-based shape memory alloys, *Acta Mater.* 59(17) (2011) 6620-6630.
- [68] S. Pauly, G. Liu, G. Wang, U. Kuhn, N. Mattern, J. Eckert, Microstructural heterogeneities governing the deformation of Cu_{47.5}Zr_{47.5}Al₅ bulk metallic glass composites, *Acta Mater.* 57(18) (2009) 5445-5453.

[69] R. Wei, X.L. Wang, S. Yang, F. Jiang, L. He, Formation of CuZr-based bulk metallic glass composites containing nanometer-scale B2-CuZr phase through sub-T_g annealing, *J. Alloys Compd.* 617 (2014) 699-706.

[70] J. Schroers, On the formability of bulk metallic glass in its supercooled liquid state, *Acta Mater.* 56(3) (2008) 471-478.

[71] S. Pauly, J. Das, N. Mattern, D.H. Kim, J. Eckert, Phase formation and thermal stability in Cu-Zr-Ti(Al) metallic glasses, *Intermetallics* 17(6) (2009) 453-462.

[72] N. Van Steenberge, A. Concustell, J. Sort, J. Das, N. Mattern, A. Gebert, S. Suriñach, J. Eckert, M.D. Baró, Microstructural inhomogeneities introduced in a Zr-based bulk metallic glass upon low-temperature annealing, *Mater. Sci. Eng., A* 491(1-2) (2008) 124-130.

[73] W.H. Wang, The elastic properties, elastic models and elastic perspectives of metallic glasses, *Prog. Mater. Sci.* 57(3) (2012) 487-656.